CALIFORNIA STATE UNIVERSITY, NORTHRIDGE

ON THE CHARACTERIZATION OF SINGLE-EVENT RELATED BRAIN ACTIVITY FROM FUNCTIONAL MAGNETIC RESONANCE IMAGING (FMRI) MEASUREMENTS

A thesis submitted in partial fulfillment of the requirements
for the degree of Master of Science
in Mathematics

by

Nafiseh Khoram

December 2013

The thesis of Nafiseh Khoram is approved:

Pierluigi Falco, Ph.D.	Date
Vladislav Panferov, Ph.D.	Date
Rabia Djellouli, Ph.D., Chair	Date

California State University, Northridge

Dedication

I would like to dedicate this work to my parents, my brother and all my friends in and outside of the country. Their love and support was what took me through this process and made this accomplishment possible.

Acknowledgements

First I would like to thank my parents and my brother for always being supportive in all my decisions and life situations, and always encouraging me to succeed in my academic life and other aspects as well.

I would like to thank my advisor Dr. Rabia Djellouli for all his support and guidance throughout this journey. I would also like to thank my committee members Dr. Vladislav Panferov and Dr. Pierluigi Falco for their constructive comments, remarks and suggestions.

Also, I would like to thank IRIS for providing financial support, which made it possible to do this project.

Table of Contents

ABSTRACT

ON THE CHARACTERIZATION OF SINGLE-EVENT RELATED BRAIN ACTIVITY

FROM FUNCTIONAL MAGNETIC RESONANCE IMAGING (FMRI)

MEASUREMENTS

By

Nafiseh Khoram

Master of Science in Mathematics

The goal of this study is to design a numerical procedure for calibrating the mathematical model that describes single-event related brain response when fMRI measurements are given. This problem can be formulated as an inverse problem that falls in the category of parameter identification of a dynamical system. We have analyzed this problem mathematically and have established results pertaining to the sensitivity of the response to the biophysiological parameters. From a numerical point of view, we have designed a regularized iterative method equipped with Kalman filtering method to estimate these parameters from the knowledge of some fMRI measurements. The Newton component of the proposed algorithm addresses the nonlinear aspect of the problem. The regularization procedure is used to ensure the stability of the algorithm. The de-noising procedure is incorporated to address the noise in the model. We have employed this method to estimate the biophysiological parameters of the so-called Balloon model which is a dynamical system that describes the hemodynamic brain responses. More specifically, we have performed a numerical investigation using synthetic data tainted with various noise levels to assess the performance of the proposed method. The obtained results illustrate the potential of the proposed solution methodology to accurately and efficiently estimate the biophysiological parameters. In addition, these results indicate that the proposed method outperforms the Cubature Kalman Filter (CKF), a procedure that has been developed recently and is considered to be one of the most successful parameter estimation techniques. Finally,

using real fMRI measurements obtained from a finger tapping experiment conducted at the Nationwide Childrens Hospital, Columbus, OH, we have calibrated the corresponding Balloon model and have estimated its biophysiological parameters.

Chapter 1

Introduction

The human brain is a network of about one trillion neurons with one thousand trillion connections, making it one of the most complex systems in the universe. Mapping the structure of the human brain is a daunting task. Indeed, tracing or analyzing these connections in an area of just one millimeter square of tissue can take years. Allowing researchers and physicians to visualize the architecture of the brain is a recognized scientific need of pressing importance since, as it is well-known, physical and psychological disorders can be detected by studying the changes in the anatomy, physiology, and chemistry of the brain. When the brain cannot effectively coordinate the billions of cells in the body, the results can adversely affect many aspects of life. Scientists are continually learning more about how the brain grows and works in healthy people, and how normal brain development and function can go awry, leading to illnesses. Neurology has grown leaps and bounds in recent times. In spite of this tremendous progress, very little is known about the brain, as president Obama unveiled his proposal for a federal brain mapping project earlier this year, he said about the brain: "There is this enormous mystery waiting to be unlocked" [38].

One of the reasons the brain has been a mystery for so long is that it is encased in the skull. Under ordinary circumstances, one does not have easy access to seeing the brain. Being able to see into the human body took a big leap forward when Wilhelm Roentgen discovered x-rays [34]. However, being encased by the skull, the brain and other soft tissues were still unknown territory for physicians and physiologists. Nowadays, physicians have a wide array of tools to understand this enigmatic organ, thanks to the interdisciplinary efforts made by science, engineering, and mathematics. Examples of these imaging techniques include two-dimensional cross sections of the brain. These systems allow static views of the brain. It also allows to make movies that show the dynamic of the brain. The recent invention of fMRI, appear to be a powerful tool for providing three-dimensional images of the brain which allows physicians to detect the activated regions of the brain. This advancement open widely a new horizon of hope and possibilities for detecting and diagnosing many disorders such as Alzheimer's, depression, brain tumor, and strokes. The applied mathematics can and should play an important role toward this research journey for understanding brain activity.

Mathematics exploits current knowledge of the brain to provide a valuable tool for understanding the brain. It helps to understand neuronal organization and transmission of

signals (nerve conduction) between the brain and other parts of our nervous system. It uses dynamical systems in an attempt to, for example, understand epilepsy and to predict the start of seizures. Furthermore, mathematics provides modeling for various aspects of the brain to understand how to map different parts of the brain to specific brain functions.

In this study, we consider an inverse problem arising in functional brain imaging. It consists of identifying the parameters of the brain activation model from fMRI measurements. fMRI is an MRI procedure that measures brain activity by detecting associated changes in blood flow and produces 3D images of brain by detecting the Blood Oxygenation Level Dependent (BOLD) signal [26]. Since the early 1990s, fMRI has attracted widespread interest in basic and clinical research and patient care. fMRI is an essential clinical tool to assess how risky brain surgeries or similar invasive treatments are for a patient. This technique relies on the fact that cerebral blood flow (CBF) and cerebral metabolic rate of oxygen ($CMRO_2$) are coupled. When an area of the brain is in use, blood flow to that region also increases which results in an increase in the blood oxygenation level. In general, hemoglobin (Hb) is diamagnetic when oxygenated and paramagnetic when deoxygenated [4]. The changes in deoxyhemoglobin level distorts the magnetic field in the fMRI machine and creates a signal strong enough for the machine to pick up.

Recent fMRI studies have used some inversion methods, such as Dynamic Expectation Maximization (DEM) [14], Cubature Kalman Filter (CKF) [1], Sequential Monte Carlo (SMC) [11]. The results reported in [24] are very promising and tend to indicate that CKF is currently one of the most successful methods. Nevertheless, as it is demonstrated in Chapter 6, this method fails to determine accurately the biophysiological parameters in the absence of a priori knowledge on the values of these parameters.

The main goal of our effort is to propose a new approach to invert (fit) models of coupled dynamical systems. This method is based on a combination of Cubature Kalman filtering (CKF) and a regularized Newton algorithm (RNA). The Newton component of the proposed algorithm addresses the nonlinear aspect of the problem. The regularization procedure is used to ensure the stability of the algorithm. The de-noising procedure is incorporated to address the noise in the model. The results reported in Chapter 6 demonstrate the efficiency (cost-effectiveness and accuracy) of the proposed solution methodology, as well as its stability and its robustness to the noise effect. Moreover, the results clearly indicate the convergence of the proposed algorithm even when starting with blind initial guesses.

The remainder of this manuscript is organized as follows. In chapter 2, we introduce the concept of forward and inverse problems and their properties. In chapter 3, we state the

mathematical model (the forward problem) that describes the changes in the physiological properties of the brain (brain responses) to exogenous stimulus during brain activation. We also formulate the parameter estimation problem (the inverse problem) that consists of finding the biophysiological parameters of this model from the knowledge of fMRI measurements. In Chapter 4, we present the obtained mathematical results on the sensitivity of the brain responses to the sought-after biophysiological parameters. Chapter 5 is devoted to the description of the features of the proposed inversion algorithm. In Chapter 6, we assess the performance of the designed algorithm. We present the results of two sets of numerical experiments with synthetic data. The first set corresponds to a Gaussian control input, whereas the second one corresponds to an on-off control input. In Chapter 7, we present model calibration results using real fMRI measurements corresponding to a finger tapping experiment. Summary and concluding remarks are presented in the conclusion section. Finally, a brief description on how fMRI provides images of the brain is included, for completeness, in the attached appendix.

Chapter 2

Preliminary Definitions and Concepts

2.1 Forward and Inverse Problems

Generally, given a complete description of a physical system, we can predict the outcome of some measurements. This problem of predicting the result of measurements is called the *modelization problem*, the *simulation problem*, or the *forward problem*. The *inverse problem* consists of using the actual result of some measurements to infer the values of the parameters that characterize the system. While the forward problem has a unique solution, the inverse problem does not [46].

We consider a physical system where variables and parameters interact in a domain of interest. Variables are physical quantities that are observable or measurable, and their values change with position and time to form signals. We may express system structures and properties as parameters, which may also change with position and time. For a given system, we understand its dynamics based on underlying physical principles describing the interactions among the variables and parameters. We adopt mathematical tools to express the interactions in a manageable way [28].

A mathematical representation of the system dynamics is the forward problem formulation. We formulate the forward problem of the system in Figure 2.1 as

$$y = \mathcal{F}(x, u, p) \tag{2.1}$$

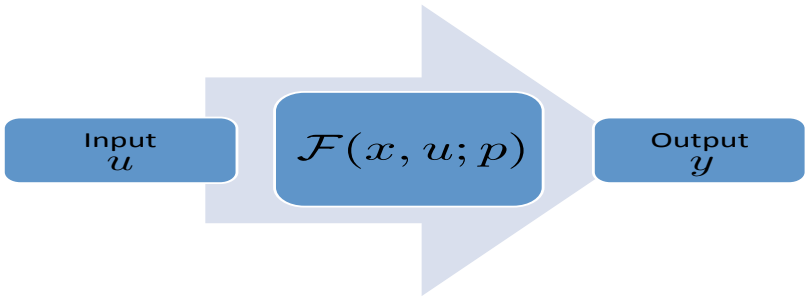

Figure 2.1: Forward problem for a system with parameter p, input u, state variable x and output y.

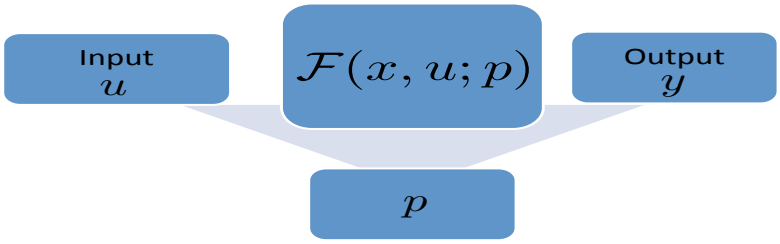

Figure 2.2: Inverse problem to find system parameter p, state variable x from input u, and output y.

where, $\mathcal{F}$ is a linear or nonlinear function that describes the relation between system parameter p, input u, variable x and output y.

For a given forward problem we consider the inverse problem to find the system parameters p from the state variable x, a designed input u and measured output y.

We formulate the inverse problem in Figure 2.2 as

$$p = \mathcal{F}^{\dagger}(x, u; y) \tag{2.2}$$

where, $\mathcal{F}^{\dagger}$ is the linear or nonlinear operator defining the inverse problem of finding the parameters of the system.

In general, most inverse problems are challenging, since the dynamics among inputs, outputs and system parameters are attributed to complex, possibly nonlinear, physical phenomena. Within a given measurement condition, multiple inputs may result in the same output for given system parameters. Similarly, different system parameters may produce the same input-output relation. The inversion process, therefore, suffers from the uncertainty that originates from the mixing process of the corresponding forward problem [28].

Inverse problems are particularly useful, because they give us information about the unknown parameters in the system that we cannot directly observe. However, the estimation process is typically ill-posed in the sense that noise in the data may give rise to significant errors in the estimate [48]. In §2.2 we will bring the definition of a well-posed and an ill-posed problem in more details. To deal with this ill-posed problems many techniques have been developed. In §2.3, we briefly review some mathematical techniques that are frequently used for rigorous analysis and investigation of quantitative properties in forward and inverse problems [28].

Inverse problems are ill-posed when measurable data are either insufficient for uniqueness or insensitive to perturbations of parameters to be imaged. To solve an inverse problem in a robust way, we should adopt a reasonably well-posed modified model at the expense of a reduced spatial resolution and/or add additional a priori information. Finding a well-posed model subject to practical constraints of measurable quantities requires deep knowledge about various mathematical theories in partial differential equations (PDEs) and functional analysis, including uniqueness, regularity, stability, layer potential techniques, micro-local analysis, regularization, spectral theory and others [28].

2.2 Well-posed and Ill-posed Problems

This section is a brief introduction to the foundations of the theory of ill-posed problems. The theory of ill-posed problems was developed in the 1960s by several mathematicians, mostly Soviet and American, but the concept of ill-posed problems goes back to J. Hadamard[1] in the beginning of 20^{th} century in the attempt to clarify what types of boundary conditions are most natural for various types of differential equation (for example, the Dirichlet and analogous problems for elliptic equations and the Cauchy problem for hyperbolic equations) [47]. We begin with abstract definitions of well-posedness, ill-posedness.

Let A be an operator and X and Y two topological spaces such that $A : X \to Y$. The topological spaces X and Y are determined by the formulation of the problem. Throughout what follows, $D(A)$ is the domain of definition and $R(A)$ is the range of A. Consider the equation,

$$Ax = y, \quad x \in X, \quad y \in Y, \tag{2.3}$$

where x is the sought solution, y is a given right-hand side, X and Y are some topological spaces, and A is a given continuous operator (linear, nonlinear, algebraic, differential, integral, etc.)

Definition 2.2.1 (Well-posed problem)**.** *The problem of solving Eq.* (2.3) *presents a well-posed problem on the pair of topological spaces X and Y if the following three conditions hold:*

1. *For any $y \in Y$, there exists an element $x \in X$ such that $Ax = y$, i.e., $R(A) = Y$ (The existence condition),*

[1] Jacques Salomon Hadamard (8 Dec. 1865-17 Oct. 1963) was a French mathematician who made major contributions in number theory, complex function theory, differential geometry and partial differential equations.

2. *The solution $x \in X$ to the equation $Ax = y$, is uniquely determined by the element $y \in Y$, i.e., the inverse operator A^{-1} exists (The uniqueness condition),*

3. *the solution x depends on y continuously, i.e., the inverse operator A^{-1} is a continuous operator (The stability condition).*

The definition of well-posedness according to Hadamard is also called the *classical definition of well-posedness*.

Definition 2.2.1 can be made more specific by replacing the topological spaces X and Y by metric, Banach, Hilbert, or Euclidean spaces. In some cases, it is reasonable to take a topological space for X and a Euclidean space for Y , and so on. The only fixed requirements in the definition are the existence, uniqueness, and stability of the solution [30].

Definition 2.2.2 (Ill-posed problem)**.** *A problem is ill-posed if at least one of the three well-posedness conditions does not hold.*

Examples of typical well-posed problems include the Dirichlet problem for Laplace's equation, and the heat equation with specified initial conditions. These might be regarded as *natural* problems that is there are physical processes that solve these problems. By contrast the inverse heat equation, deducing a previous distribution of temperature from final data is not well-posed that is the solution is highly sensitive to changes in the final data.

Such continuum problems must often be discretized in order to obtain a numerical solution. While in terms of functional analysis such problems are typically continuous, they may suffer from numerical instability when solved with finite precision, or with errors in the data. If the problem is well-posed, then it stands a good chance of solution on a computer using a stable algorithm. If it is not well-posed, it needs to be re-formulated for numerical treatment. Typically this involves including additional assumptions, such as smoothness of solution. This process is known as regularization. Tikhonov regularization is one of the most commonly used method for regularization of linear ill-posed problems.

In fact, many applied problems (in signal and image processing, tomography, spectroscopy, control theory, etc.) are ill-posed problems, which fact was widely recognized in several last decades [50].

2.3 Methods for Solving Inverse Problems

When solving an inverse problem, the main two issues to be addressed are the uniqueness and the stability. If the uniqueness is satisfied, then the existence of the solution will follow from restricting the considered operator to its range. On the other hand, if a solution is not unique, we must check its optimality in terms of its physical meaning and practical usefulness. The stability is crucial since one wants to make sure that small errors in the data (which are, in practice, measured quantities) will cause only small errors in the solution [28], [9].

There is no universal method for solving ill-posed problems. In every specific case, the main trouble instability has to be tackled in its own way [30]. The problem for solving an equation can be a well- or ill-posed problem depending on the particular types of the functional spaces in which the solution is sought and the initial conditions are set. Moreover, different types of equations display different degree of ill-posedness [50].

If we can properly formulate the forward problem of a physical system and also its inverse problem, we can safely assume that a solution exists. Non-uniqueness often becomes a practically important issue, since it is closely related with the inherent mixing process of the forward problem. Once the inputs are mixed, uniquely sorting out some inputs and system parameters may not be feasible. The mixing process may also cause sensitivity problems. When the sensitivity of a certain output to the inputs and/or system parameters is low, small changes in the inputs or system parameters may result in small and possibly discontinuous changes in the output, with measurement errors. The inversion process in general includes a step where the measured output values are divided by sensitivity factors. If we divide small measured values, including errors, by a small sensitivity factor, we may amplify the errors in the results. The effects of the amplified errors may easily dominate the inversion process and result in useless solutions, which do not comply with the continuity requirement [28].

Considering that mixing processes are embedded in most forward problems and that the related inverse problems are ill-posed in many cases, we need to devise effective methods to deal with such difficulties. One may incorporate as much a priori information as possible in the inversion process. Preprocessing methods such as de-noising and feature extraction can be employed. One may also need to implement some regularization techniques to find a compromise between the robustness of an inversion method and the accuracy or sharpness of its solution [28].

Since most inverse problems cannot be solved analytically, computational methods play a fundamental role [48].However, the solution of ill-posed problems does not depend

continuously on the data, therefore small errors, whether round off errors, or measurement errors, or perturbations caused by noise, can create large deviations in the solutions. Therefore the numerical treatment of ill-posed problems is a challenge [45].

The choice of the treatment for an ill-posed problem depends on the problem itself and the set of data.

Chapter 3

Brain activity: The Mathematical Study

Functional magnetic resonance imaging (fMRI) has been the area of great interest among the functional brain imaging techniques. Its main features: noninvasiveness, radiation free, and good temporal and spatial resolution, have made it the standard in brain activity measurement. The contrast agent in fMRI, the Blood Oxygenation Level Dependent (BOLD) signal ([39], [40]), is induced by decreases in the deoxyhemoglobin content in the active region of the brain. Measuring the BOLD allows to track indirectly changes in the blood flow.

Expressing the observed phenomena of the BOLD signal as the output of a mathematical model, was one of the most challenging tasks in the early fMRI studies. Two main approaches have been adopted to describe the hemodynamic response of the brain: the General Linear Modeling (GLM) and the nonlinear modeling frameworks. In the GLM approach, statistical analysis tools are used to assess the convolution of the neural activity signal with a predefined convolution kernel, called Hemodynamic Response Function (HRF). Several basis functions have been used as HRF such as Poisson function ([16]), Gaussian function ([42]), Gamma function ([15], [7]) and inverse Logit function ([33]). This approach is blind to the physiological aspects that underlie the BOLD transients and has the main drawback of excluding the nonlinear effects of the BOLD shown by [3], [5] and [17, 19].

This has motivated the emergence of nonlinear biophysical modeling approaches, among which the best known is the pioneer work of [5]. The original work proposed a dependence of the BOLD signal on variations of the normalized cerebral blood flow, volume and deoxyhemoglobin content and has been completed by [35]. The model presents the venous compartment's structure as a balloon where a stimulus resulting in a local neuronal activity leads to an increase in the blood flow. This increase exceeds the cerebral metabolic rate of oxygen thus reducing the concentration of deoxyhemoglobin which in turn results in an increase in the magnetic resonance signal. The missing relationship between the neural activity and the cerebral blood flow dynamics was introduced by [19]. Indeed, under the assumption of a linear relation between the synaptic activity and the regional cerebral blood flow, a new variable called the flow-inducing signal has been introduced. The proposed coupling between the neuronal activity and the cerebral blood flow has a linear second order behavior.

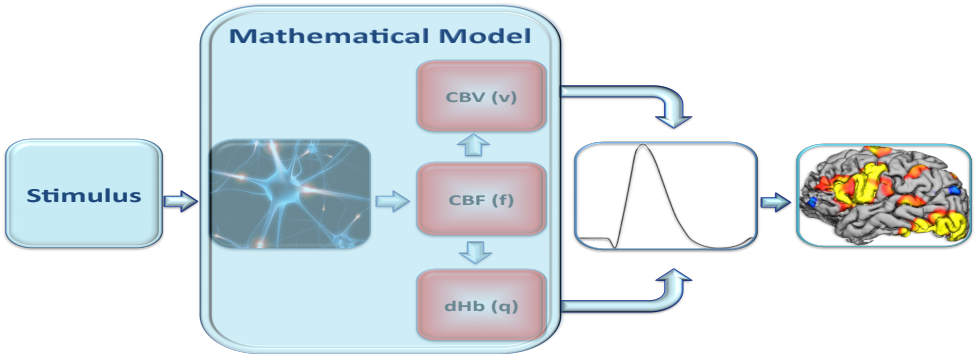

Figure 3.1: Mathematical model

In this chapter we introduce the mathematical model that describes the changes in the hemodynamic properties of the brain during activation in the form of s dynamical system. We then formulate the inverse problem to find the unknown parameters involved in the mentioned dynamical system as a parameter estimation problem. We also analyze this model from a mathematical point of view by proving the uniqueness of the solution the inverse problem, as well as introducing a vigorous algorithm to solve this inverse problem for given fMRI measurements.

3.1 The Hemodynamical Model: The Direct Problem

Nonlinear filtering problems are typically described by state-space models comprising a process and measurement equation. In many practical problems, the process equation is derived from the underlying physics of a continuous dynamic system, and is expressed in the form of a set of differential equations. Since the measurements y are acquired by digital devices; i.e., they are available at discrete time points ($t = 1, 2, \ldots, T$), we have a model with a continuous process equation and a discrete measurement equation [19]. The stochastic representation of this state-space model, with additive noise, can be formulated as:

$$\begin{cases} \dot{x}(t) = & A(x(t), u(t), \theta) + v_t & \text{(Process equation)} \\ y(t) = & H(x(t), \theta) + w_t & \text{(Measurement equation)} \end{cases} \tag{3.1}$$

where A is a nonlinear operator that describes the dynamics of the system. This operator is describe in §3.1.1. The explicit form of A is given in §3.1.3. Also, operator H models the measurements i.e., the BOLD signal, which will be explained in §3.1.2. Vector $\vec{x}$ represents the state variable vector, $u(t)$ is the control input function and $\vec{\theta}$ contains the parameters of the model. Random variables v and w are Gaussian white noises, that is,

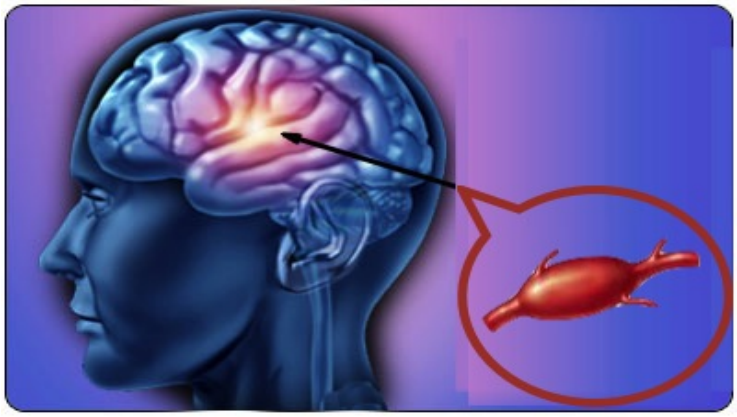

Figure 3.2: Expanded venous "balloon".

$v_t \sim \mathcal{N}(0, Q), w_t \sim \mathcal{N}(0, R)$, where Q and R are the error covariance matrices for the system and the measurements, respectively.

3.1.1 The Balloon model

After stimulation, there is an increased neuronal activity in some part(s) of the brain. This neuronal activity evokes an increase in oxygen and glucose consumption supplied by the vascular system. Therefore, blood flow increases to make up for the lack of oxygen used by the activated cells. The vascular bed within a small volume of tissue is then modeled as an expandable venous compartment. The increase in the blood flow, inflates a venous "balloon" causing an increase in the blood volume and decrease in the deoxyhemoglobin content level in the blood. The balloon model, explains the dynamic of blood volume and deoxyhemoglobin content called hemodynamic brain responses.

The Balloon model [5] is an input-state-output model with two state variables volume v and deoxyhemoglobin content q. This is a simple and plausible model that is predicated on a minimal set of assumptions [20]. The volume flow rate (ml/s) into the tissue, F_{in}, is an assumed function of time that drives the system. The volume flow out, F_{out}, is assume to primarily depend on the pressure in the venous compartment and the resistance of the vessels after the balloon. However, rather than introducing the pressure explicitly into the equations and thus introducing more parameters to the system, F_{out} is assumed to be a function of the venous volume V. This is an empirical relation studied by [21] and [35]. The rate of change of the volume of the balloon is the difference between F_{in} and F_{out} [5].

$$\frac{dV}{dt} = F_{in}(t) - F_{out}(v) \tag{3.2}$$

and the rate of deoxyhemoglobin is,

$$\frac{dQ}{dt} = F_{in}(t)E\,C_a - F_{out}(v)\frac{Q(t)}{V(t)} \tag{3.3}$$

where, $Q(t)$ is the total deoxyhemoglobin in the tissue element, E is the net extraction of O_2 concentration, C_a is the arterial O_2 concentration, and $F_{out}(v) \times Q(t)/V(t)$ is the clearance rate of deoxyhemoglobin from the tissue ($Q(t)/V(t)$ is the average venous concentration).

By scaling each of these variables with their value at rest (t=0), we have:

$$v(t) = \frac{V(t)}{V_0},\ q(t) = \frac{Q(t)}{Q_0},\ f_{in}(t) = \frac{F_{in}(t)}{F_0},\ f_{out}(v) = \frac{F_{out}(V)}{F_0}. \tag{3.4}$$

Therefore, Eqs. (3.2) and (3.6) will be:

$$\tau_0\frac{dv}{dt} = f_{in}(t) - f_{out}(v) \tag{3.5}$$

$$\tau_0\frac{dq}{dt} = f_{in}(t)\frac{E(f_{in}, E_0)}{E_0} - f_{out}(v)\frac{q(t)}{v(t)} \tag{3.6}$$

Equation (3.5) says that volume changes reflect the difference between inflow f_{in} and outflow f_{out} from the venous compartment with a time constant τ_0. This constant represents the mean transit time (i.e., the average time it takes to traverse the venous compartment or for that compartment to be replenished) and is V_0/F_0, where F_0 is resting flow.

Note that outflow is a function of volume. This function models the balloon-like capacity of the venous compartment to expel blood at a greater rate when distended. It is modeled with a single parameter α based on the windkessel model,

$$f_{out} = v^{1/\alpha} \tag{3.7}$$

The physiology of the relationship between flow and volume is determined by the evolution of the transit time. Mandeville1999 et al. [35] reformulated the temporal evolution of transit time into a description of the dynamics of resistance and capacitance of the balloon using windkessel theory (wind- kessel means leather bag). This enabled them to posit a form for the temporal evolution of a downstream elastic response to arteriolar vasomotor changes and estimate mean transit times using measurements of volume and flow, in rats, using fMRI and laser-Doppler flowmetry. In Eq. (3.7), $1/\alpha = \gamma+\beta$. $\gamma = 2$ represents laminar flow. $\beta > 1$ models diminished volume reserve at high pressures and can be thought of as the ratio of the balloons capacitance to its compliance. At steady state empirical results from PET suggest $\alpha \approx 0.38$ [21]. However, when flow and volume are changing dynamically, this value is smaller. [35] were the first to measure the dynamic flow-volume relationship and estimated $\alpha \approx 0.18$, after 6 s of stimulation, with a projected asymptotic (steady-state) value of 0.36.

Eq. (3.6), represents the change in deoxyhemoglobin, which reflects the delivery of deoxyhemoglobin into the venous compartment minus that expelled (outflow times concentration). The term, E(f_{in}, E_0), in Eq. (3.6), is the fraction of oxygen extracted from the inflowing blood. This is assumed to depend on oxygen delivery and is consequently flow dependent. A reasonable approximation for E(f_{in}, E_0) is given by [5],

$$E(f_{in}, E_0) = 1 - (1 - E_0)^{1/f_{in}} \tag{3.8}$$

The second term in Eq. (3.6) represents an important nonlinearity: The effect of flow on signal is largely determined by the inflation of the balloon, resulting in an increase of $f_{out}(v)$ and clearance of deoxyhemoglobin. This effect depends upon the concentration of deoxyhemoglobin such that the clearance attained by the outflow will be severely attenuated when the concentration is low (e.g., during the peak response to a prior stimulus).

This concludes the Balloon model component, where there are only three unknown parameters that determine the dynamics E_0, τ_0, and α, namely resting oxygen extraction fraction (E_0), mean transit time (τ_0), and a stiffness exponent (α) specifying the flow-volume relationship of the venous balloon. The only thing required, to specify the BOLD response, is inflow [20] that is chosen to be,

$$\frac{df_{in}}{dt} = s(t) \tag{3.9}$$

where s is some flow inducing signal defined, operationally, in units corresponding to the rate of change of normalized flow (i.e., s^{-1}).

The signal is assumed to subsume many neurogenic and diffusive signal subcomponents and is generated by neuronal activity $u(t)$,

$$\frac{ds}{dt} = \epsilon u(t) - s(t)/\tau_s - (f_{in}(t) - 1)/\tau_f \tag{3.10}$$

ϵ, τ_s, and τ_f are the three unknown parameters that determine the dynamics of this component of the hemodynamic model. They represent the efficacy with which neuronal activity causes an increase in signal (ϵ), the time-constant for signal decay or elimination (τ_s), and the time-constant for auto-regulatory feedback from blood flow (τ_f). Therefore, the Balloon model is given by the following set of equations:

$$\begin{cases} \dot{f}_{in}(t) = s(t) & \text{(3.11a)} \\ \dot{s}(t) = \epsilon u(t) - \mathcal{K} s(t) - \mathcal{X}(f_{in}(t) - 1) \quad ; \mathcal{K} = 1/\tau_s, \mathcal{X} = 1/\tau_f & \text{(3.11b)} \\ \dot{v}(t) = \dfrac{1}{\tau_0}(f_{in}(t) - v(t)^{1/\alpha}) & \text{(3.11c)} \\ \dot{q}(t) = \dfrac{1}{\tau_0}(f_{in}(t)\dfrac{1 - (1 - E_0)^{1/f_{in}(t)}}{E_0} - v(t)^{\frac{1}{\alpha}-1} q(t)) & \text{(3.11d)} \end{cases}$$

3.1.2 The BOLD signal

The Balloon model describes the changes in physiological variables during brain activation. To connect the model with experimental fMRI, we first need a quantitative model for BOLD signal changes as a function of blood oxygenation level and volume. This relationship has been extensively explored in recent years using experimental data [41], numerical Monte Carlo simulations [41, 40], and analytical calculations [49, 5].

The BOLD effect is primarily due to changes in local deoxyhemoglobin content, but quantitative modeling of this effect requires some subtlety. In fact, there are two sources of signal change that must be modeled: the intravascular (S_i) and the extravascular (S_e) signals [2, 40]. Both regimes are affected by the magnetic field gradients created by the presence of deoxyhemoglobin, which cause the MR signal to decay faster when deoxyhemoglobin increases. The clearance of deoxyhemoglobin reduces intravoxel dephasing and engenders an increase in signal. [4]. These signal components depend on the deoxyhemoglobin content and render the signal a nonlinear function of v and q. The effect of flow on v and q determines the output and it is these effects that are the essence of the Balloon model. In fact, we consider the total BOLD signal to be a volume-weighted sum of the S_e and S_i signal:

$$S = (1 - V)S_e + VS_i \tag{3.12}$$

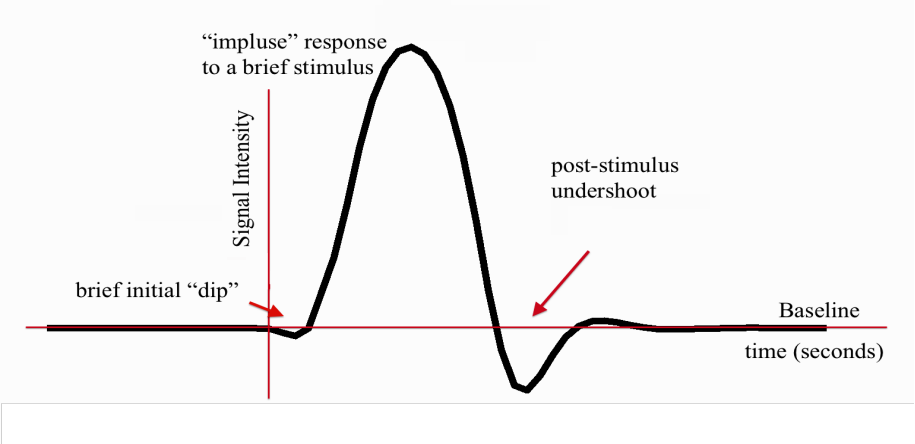

Figure 3.3: The BOLD signal

where V is the blood volume fraction. Then, for small signal changes ΔS:

$$\Delta S = (1 - V_0)\Delta S_e - \Delta V S_e + V_0 \Delta S_i + \Delta V S_i \tag{3.13}$$

where V_0 is the resting blood volume fraction. Combining numerical results from [40] and Eq. (3.13) we get the following form for the BOLD signal:

$$y(t) = \frac{\Delta S}{S} = V_0 \left[k_1(1 - q(t)) + k_2(1 - \frac{q(t)}{v(t)}) + k_3(1 - v(t)) \right] \tag{3.14}$$

where v and q are the normalized blood volume and deoxyhemoglobin content, respectively. (i.e., $v = V/V_0, q = Q/Q_0$ and $q = v = 1$ at rest).

The first term describes the intrinsic extravascular signal, the second term describes the intravascular signal, and the third term describes the effect of changing the balance of the sum in Eq. (3.12). The parameters k_l, k_2 and k_3 are scanner-dependent and dimensionless. Based on the numerical studies of [40] and [2], for a $1.5T$ scanner and TE[1] $= 40\,ms$, they have been estimated to $k_1 = 7E_0, k_2 = 2$ and $k_3 = 2E_0 - 0.2$, where E_0 is the resting oxygen extraction fraction [5].

[1]TE is the Echo Time. It represents the time in milliseconds between the application of the 90° pulse and the peak of the echo signal in Spin Echo and Inversion Recovery pulse sequences (`http://fonar.com/glossary.htm`, accessed October 25, 2013).

The BOLD response is qualitatively the inverse of the total deoxyhemoglobin response. Before the balloon has inflated sufficiently the expulsion and dilution may be insufficient to counteract the increased delivery of deoxygenated blood to the venous compartment and an early dip in signal may be expressed. After the flow has peaked, and the balloon has relaxed again, reduced clearance and dilution contribute to the post stimulus undershoot commonly observed, as illustrated in Figure 3.3 [5].

Throughout what follows we consider the state vector consisted of f, s, v and q. And the unknown parameters are $\epsilon, \mathcal{K}, \mathcal{X}, \tau_0, E_0, \alpha$ and V_0. For simplicity in our analysis we let the state vector $\vec{x} = (x_1(t), x_2(t), x_3(t), x_4(t)) = (f(t), s(t), v(t), q(t))$ representing the state variables (see Table 3.1) and $\vec{\theta} = (\theta_1, \theta_2, \theta_3, , \theta_4, \theta_5, \theta_6, \theta_7) = (1/\alpha, \epsilon, \mathcal{K}, \mathcal{X}, \tau_0, E_0, V_0)$ representing the parameters (see Table 3.2).

State variables	Description	Value at rest
x_1	Cerebral blood flow (f)	1
x_2	Flow inducing signal(s)	0
x_3	Cerebral blood volume (v)	1
x_4	Total deoxyhemoglobin content level (q)	1

Table 3.1: Description of state variables

Descriptions	Biophysiological parameters	Typical values
Stiffness exponent (α)	$(\theta_1)^{-1}$	.34
Neural efficacy (ϵ)	θ_2	.54
Rate of signal decaying ($\mathcal{K}$)	θ_3	.65
Rate of flow-dependent elimination ($\mathcal{X}$)	θ_4	.38
Hemodynamic transit time (τ)	θ_5	.98
Resting net oxygen extraction fraction (E_0)	θ_6	.32
Resting blood volume (V_0)	θ_7	.04

Table 3.2: Description of the parameters

3.1.3 Hemodynamical system

The problem of describing the single-event related hemodynamic brain response to an exogenous input can be described in the framework of the dynamical system theory. The model we consider in this section is called hemodynamical system (HDS). This mathematical model has been first introduced by [5] and then revisited by [20] to account for the nonlinearities involved in the process and measurement equations [24]. This hemodynamical system (HDS) is a first order nonlinear differential system given by:

$$(HDS) \quad \begin{cases} \dot{\vec{x}}(t) = & A(\vec{x}(t), \vec{\theta}, u(t)) + v_t \\ y(t) = & H(\vec{x}(t), \vec{\theta}) + w_t \\ \vec{x}(0) = & \vec{x}_0 \end{cases} \quad ; t \geq 0 \tag{3.15}$$

where the nonlinear function A is given by:

$$A(\vec{x}(t), u(t), \vec{\theta}) = \begin{cases} x_2(t) & \text{(3.16a)} \\ \theta_2 u(t) - \theta_3 x_2(t) - \theta_4(x_1(t) - 1) & \text{(3.16b)} \\ \theta_5(x_1(t) - x_3(t)^{\theta_1}) & \text{(3.16c)} \\ \theta_5(x_1(t)\dfrac{1 - (1 - \theta_6)^{1/x_1(t)}}{\theta_6} - x_4(t)x_3(t)^{(\theta_1 - 1)}) & \text{(3.16d)} \end{cases}$$

and the function H is given by:

$$H(\vec{x}(t), \vec{\theta}) = \theta_7 \left[k_1(1 - x_4(t)) + k_2(1 - x_4(t)/x_3(t)) + k_3(1 - x_3(t))\right] \tag{3.17}$$

- The first equation of HDS describes the underlying physics of the continuous hemodynamic system, that is, the Balloon model.
- The second equation of HDS models the observations, that is, the Blood Oxygenation Level Dependent (BOLD) signal.
- The third equation of HDS is the initial conditions indicating the values of the state variables at rest.
- v_t is a random vector with zero mean and 4×4 positive semidefinite covariance matrix depending on t, Q: $\mathcal{N}(0, Q)$. v_t represents the possible noise on the system, with respect to time t.
- w_t is a random variable with zero mean and non-negative real valued covariance depending on t, R: $\mathcal{N}(0, R)$. w_t represents the possible noise on the measurements, with respect to time t.

3.2 Mathematical Formulation: The Inverse Problem

The hemodynamic system HDS given by Eqs. (3.15)-(3.17), defines an operator $\mathcal{F}$ that maps the biophysiological parameters $\vec{\theta} = (\theta_1, \theta_2, \ldots, \theta_7) \in \mathbb{R}^7$ to the BOLD signal

y. Therefore, the problem of identifying the unknown parameters $\vec{\theta}$, from the knowledge of a measured BOLD signal y can be formulated as the following inverse parameter problem,

$$(IPP) \quad \begin{cases} \textit{Given an initial state } \vec{x}_0\textit{, a control input } u(t)\textit{, and a measured} \\ \textit{BOLD signal } y\textit{, find the biophysiological parameters vector } \vec{\theta} \\ \textit{such that,} \\ \mathcal{F}(\vec{\theta}; \vec{x}, u) = y \end{cases} \tag{3.18}$$

Note that (IPP) given by Eq. (3.18) is a nonlinear inverse problem that falls in the category of identifying the parameters of ordinary differential systems.

Chapter 4

Mathematical Analysis

In this section we provide a mathematical analysis based on the Balloon model [5] which is a first step to show the uniqueness of the solution to the problem (3.18). To do so, we first go through some calculations and then bring the numerical results in the next chapters. In our analysis we use two types of control inputs:

- A *Gaussian* input given by:

$$u(t) = 2\exp(-(t-\mu)^2/2\sigma^2) \tag{4.1}$$

  where, μ and σ are positive numbers representing the mean and standard deviation respectively.

- A step function also called the *On-Off* input:

$$u(t) = \begin{cases} 0 & 0 \leq t < t_1 \\ 1 & t_1 \leq t \leq t_2 \\ 0 & t_2 < t \leq t_f \end{cases} \tag{4.2}$$

  where the interval $[t_1, t_2]$ is the time period of applying the stimulus, and t_f is the duration of the experiment.

4.1 The Main Result: A Uniqueness Theorem

The question that if the inverse problem given by IPP admits a unique solution, $\vec{\theta}$ has been a controversial question. To answer this question, we conducted a mathematical analysis to show the injectivity of the operator $\mathcal{F} : \vec{\theta} \to y$. To this end, we adopt throughout this section the following assumptions: Throughout this section we assume:

$$(*) \begin{cases} \bullet \text{ The initial state } \vec{x}_0 \text{ is given by: } \vec{x}_0 = [1,0,1,1]^T \\ \bullet \text{ The control input } u(t) \text{ is a square function given by Eq. (4.2).} \\ \bullet \text{ The system is noise-free, that is, } v_t = w_t = 0. \\ \bullet \text{ The solution } \vec{x} \text{ to the HDS given by Eqs. (3.15)-(3.17) exists on } [0, t_f]. \end{cases}$$

Theorem 1. *Let Θ be the space of admissible system parameters, and $\mathcal{X}$ be the space of solution to the HDS* (3.15)*. Then the mapping $\mathcal{F}_1 : \vec{\theta} \to \vec{x}$ from Θ to $\mathcal{X}$ is a one-to-one*

mapping.

4.2 Proof of the Main Result

We prove Theorem 1 in four steps. Each step is formulated as a proposition. To this end, we first state and prove the following technical result.

Lemma 1.1. *Let a be a positive real number such that $a \neq 1$. Consider the function:*

$$f_a(x) = \frac{1-(1-x)^a}{x}; \qquad 0 < x < 1 \tag{4.3}$$

Then, f_a is a one-to-one function on $(0,1)$.

Proof. We prove that f_a is a monotonic function. Since f_a is differentiable, the monotonicity of f_a follows from showing that $f'_a(x)$ has a constant sign on $(0,1)$. We have:

$$f'_a(x) = \frac{(1-x)^a + ax(1-x)^{a-1} - 1}{x^2}; \quad x \in (0,1) \tag{4.4}$$

We set

$$g_a(x) = ax(1-x)^{a-1} + (1-x)^a - 1; \quad x \in (0,1) \tag{4.5}$$

Hence, the sign of f'_a is the sign of g_a. On the other hand, we have:

$$g'_a(x) = -a(a-1)x(1-x)^{a-2} \tag{4.6}$$

If $a > 1$, then $g'_a(x) < 0$, whereas if $0 < a < 1$, then $g'_a(x) > 0; \forall x \in (0,1)$.
Since $g_a(0) = 0$, then it follows that if $a > 1$, then g_a is negative on $(0,1)$, whereas if $0 < a < 1$, then g_a is positive on $(0,1)$. □

Proposition 1.1. *Let $\vec{x}$ be the solution to the HDS given by Eqs.* (3.15)-(3.17)*. Then, under the assumptions given by* $(*)$*, the vector coordinates $t \to x_j; j = 1,2,3$ are non-constant functions on $[0, t_f]$.*

Proof.

a) First assume $t \to x_1(t)$ to be a constant function on $[0, t_f]$. Then,

$$x_1(t) = 1; \quad \forall t \in [0, t_f], \tag{4.7}$$

and

$$\dot{x}_1(t) = 0; \quad \forall t \in [0, t_f]. \tag{4.8}$$

Therefore, it follows from Eq. (3.16a) that,

$$x_2(t) = 0; \quad \forall t \in [0, t_f]. \tag{4.9}$$

Hence, Eq. (3.16b) implies that,

$$u(t) = 0; \quad \forall t \in [0, t_f], \tag{4.10}$$

which contradicts assumption $(*)$. Hence, $t \to x_1(t)$ cannot be a constant function on $[0, t_f]$.

b) Next, assume $t \to x_2(t)$ is a constant function on $[0, t_f]$. Then,

$$x_2(t) = 0; \quad \forall t \in [0, t_f], \tag{4.11}$$

and

$$\dot{x}_2(t) = 0; \quad \forall t \in [0, t_f]. \tag{4.12}$$

Therefore, Eq. (3.16a) and assumptions $(*)$ ensure that:

$$x_1(t) = 1; \quad \forall t \in [0, t_f]. \tag{4.13}$$

Consequently, it follows from Eq. (3.16b) that

$$u(t) = 0; \quad \forall t \in [0, t_f], \tag{4.14}$$

which contradicts assumption $(*)$. Hence, $t \to x_2(t)$ cannot be a constant function on $[0, t_f]$.

c) Let $t \to x_3(t)$ be a constant function on $[0, t_f]$ then,

$$\dot{x}_3(t) = 0; \quad \forall t \in [0, t_f]. \tag{4.15}$$

Note that, $\theta_5 \neq 0$, otherwise it follows from Eqs.(3.16c), (3.16d), and assumptions $(*)$ that:

$$x_3(t) = x_4(t) = 1; \quad \forall t \in [0, t_f]. \tag{4.16}$$

Consequently,

$$\vec{x}(t) = \vec{x}_0 \quad \text{and} \quad y(t) = 0; \quad \forall t \in [0, t_f]. \tag{4.17}$$

Hence, the output is constantly zero which contradicts the stimulus application effect. Therefore, Eq. (3.16c) gives that:

$$x_1(t) - x_3^{\theta_1}(t) = 0; \quad \forall t \in [0, t_f] \tag{4.18}$$

Hence, we deduce from Eq. (5.12) and assumptions $(*)$ that:

$$x_1(t) = 1; \quad \forall t \in [0, t_f], \tag{4.19}$$

which contradicts part (a). Therefore, $t \to x_3(t)$ cannot be a constant function on $[0, t_f]$. □

Proposition 1.2. *Under the assumptions given by* $(*)$*, the biophysiological parameters* θ_2, θ_3 *and* θ_4*, solution of the inverse parameter problem IPP are unique.*

Proof. Let $t = t_1$, where t_1 is defined in Eq. (4.2). It follows from HDS, Eq. (3.16b) and assumptions given by $(*)$ that:

$$\dot{x}_2(t_1) = \theta_2 - \theta_3 x_2(t_1) - \theta_4(x_1(t_1) - 1) \tag{4.20}$$

and

$$\vec{x}(t_1) = \vec{x}_0. \tag{4.21}$$

Hence,

$$\theta_2 = \dot{x}_2(t_1). \tag{4.22}$$

Furthermore, it follows from HDS and Eqs. (3.16a)-(3.16b) that:

$$\ddot{x}_2(t) = -\theta_3 \dot{x}_2(t) - \theta_4 x_2(t); \quad \forall t \in (t_1, t_2] \tag{4.23}$$

where t_1 and t_2 are defined in Eq. (4.2).

Therefore, for any $t', t'' \in (t_1, t_2)$ we have:

$$\begin{bmatrix} -\ddot{x}_2(t') \\ -\ddot{x}_2(t'') \end{bmatrix} = \begin{bmatrix} \dot{x}_2(t') & x_2(t') \\ \dot{x}_2(t'') & x_2(t'') \end{bmatrix} \begin{bmatrix} \theta_3 \\ \theta_4 \end{bmatrix} \tag{4.24}$$

Observe that x_2 is a continuous function on $[0, t_f]$. Therefore, it attains its maximum at

some $t'' \in (t_1, t_2]$. Let

$$x_2(t'') = \max_{t_1 < t < t_2} x_2(t) = x_2^{max}. \tag{4.25}$$

Therefore, $\dot{x}_2(t'') = 0$. Note that, $x_2^{max} \neq 0$ because otherwise

$$x_2(t) = 0; \quad \forall t \in [0, t_f], \tag{4.26}$$

which contradicts Proposition 1.1.

Furthermore, there exists a $t' \in (t_1, t_2)$ such that $x_2(t') \neq 0$. Otherwise,

$$x_2(t) = 0; \quad \forall t \in [0, t_f], \tag{4.27}$$

which contradicts Proposition 1.1. Hence, it follows from Eq. (4.24) that:

$$\begin{bmatrix} \theta_3 \\ \theta_4 \end{bmatrix} = \begin{bmatrix} \left(x_2(t')\ddot{x}_2(t'') - x_2^{max}\ddot{x}_2(t')\right)/x_2^{max}\dot{x}_2(t') \\ -\ddot{x}_2(t'')/x_2^{max} \end{bmatrix} \tag{4.28}$$

□

Proposition 1.3. *Under the assumptions given by* $(*)$*, the biophysiological parameters* θ_1 *and* θ_5*, solution of the inverse parameter problem IPP are unique.*

Proof. Let $t^* \in (0, t_f]$ such that:

$$x_3(t^*) = \max_{0 < t \leq t_f} x_3(t) = x_3^{max}. \tag{4.29}$$

Note that t^* exists because x_3 is continuous on $[0, t_f]$. Consequently, $\dot{x}_3(t^*) = 0$. It follows from Eq. (3.16c) that:

$$\theta_5 \left(x_1(t^*) - x_3^{\theta_1}(t^*)\right) = 0. \tag{4.30}$$

Since $\theta_5 \neq 0$ (see the proof of Proposition 1.1). Then,

$$x_1(t^*) - x_3^{\theta_1}(t^*) = 0. \tag{4.31}$$

Next, we consider two cases,

Case 1: $x_3(t^*) \neq 1$. Then, we deduce from Eq. (5.14) that:

$$\theta_1 = \frac{\ln x_1(t^*)}{\ln x_3(t^*)} = \frac{\ln x_1(t^*)}{\ln x_3^{max}} \tag{4.32}$$

Case 2: $x_3(t^*) = 1$. We consider $t_* \in (0, t_f]$ such that:

$$x_3(t_*) = \min_{0<t<t_f} x_3(t) = x_3^{min}. \tag{4.33}$$

Note that $x_3^{min} \neq 1$, otherwise

$$\max_{0<t\leq t_f} x_3(t) = \min_{0<t\leq t_f} x_3(t) = 1. \tag{4.34}$$

Hence,

$$x_3(t) = 1; \quad \forall t \in [0, t_f], \tag{4.35}$$

which contradicts Proposition 1.1.

Therefore,

$$\theta_1 = \frac{\ln x_1(t_*)}{\ln x_3(t_*)} = \frac{\ln x_1(t_*)}{\ln x_3^{min}} \tag{4.36}$$

Furthermore, it follows from Eq. (3.16c) that there is at least one $\tilde{t} \in [0, t_f]$ such that:

$$x_1(\tilde{t}) - x_3^{\theta_1}(\tilde{t}) \neq 0. \tag{4.37}$$

Otherwise,

$$\dot{x}_3(t) = 0; \quad \forall t \in [0, t_f]. \tag{4.38}$$

Hence, it follows from assumptions $(*)$ that:

$$x_3(t) = 1; \quad \forall t \in [0, t_f], \tag{4.39}$$

which contradicts Proposition 1.1. We then we deduce that:

$$\theta_5 = \frac{\dot{x}_3(\tilde{t})}{x_1(\tilde{t}) - x_3^{\theta_1}(\tilde{t})} \tag{4.40}$$

□

Proposition 1.4. *Under the assumptions given by* $(*)$*, the biophysiological parameters* θ_6 *and* θ_7*, solution of the inverse parameter problem IPP are unique.*

Proof. It follows from the continuity of x_1 on $[0, t_f]$ that there is $\tilde{t} \in (0, t_f]$, such that:

$$x_1(\tilde{t}) = \max_{0<t\leq t_f} x_1(t) = x_1^{max} \geq 1. \tag{4.41}$$

Then, we obtain from Eq. (3.16d) that:

$$\dot{x}_4(\tilde{t}) = \theta_5 \left(x_1^{max} f_a(\theta_6) - x_4(\tilde{t}) {x_3}^{(\theta_1 - 1)}(\tilde{t}) \right), \tag{4.42}$$

where f_a is the function defined in Lemma 1.1 with $a = 1/x_1^{max}$. Since $\theta_5 \neq 0$ (see the proof of Proposition 1.1), then it follows from Eq. (5.2) that:

$$f_a(\theta_6) = a \left(\frac{\dot{x}_4(\tilde{t})}{\theta_5} + x_4(\tilde{t}) {x_3}^{(\theta_1 - 1)}(\tilde{t}) \right). \tag{4.43}$$

Since f_a is a one-to-one function (see Lemma 1.1), we then conclude that θ_6 is unique.

Next, we prove the uniqueness of θ_7. First, we rewrite Eq. (3.17) as follows:

$$y(t) = \theta_7 \tilde{y}(t), \tag{4.44}$$

where

$$\tilde{y}(t) = 7\theta_6(1 - x_4(t)) + 2(1 - x_4(t)/x_3(t)) + (2\theta_6 - 0.2)(1 - x_3(t)). \tag{4.45}$$

Hence, there is at least one $\hat{t} \in [0, t_f]$ such that, $\tilde{y}(\hat{t}) \neq 0$ otherwise

$$y(t) = 0; \quad \forall t \in [0, t_f], \tag{4.46}$$

which means that there is no activity. Therefore,

$$u(t) = 0; \quad \forall t \in [0, t_f], \tag{4.47}$$

which contradicts assumption $(*)$. Consequently, it follows from Eqs. (4.44) and (4.45) that:

$$\theta_7 = \frac{y(\hat{t})}{\tilde{y}(\hat{t})} \tag{4.48}$$

□

Remark 4.2.1. *Theorem 1 shows that operator $\mathcal{F}$ can be considered as $\mathcal{F} : \vec{\theta} \xrightarrow{F_1} \vec{x} \xrightarrow{F_2} y$, where operator $\mathcal{F}_1 : \vec{\theta} \to \vec{x}$ is a one-to-one function. This is the first step in proving the uniqueness of the solution to the problem of finding parameters of the HDS* (3.15) *that best describe the system output, i.e., the BOLD signal. With the result presented in Theorem 1, it remains to prove that the operator $\mathcal{F}_2 : \vec{x} \to y$ is a one-to-one mapping. However, this problem is still an ongoing work.*

4.3 Sensitivity Analysis

In this section, we provide the results pertaining to calculating the Jacobian of the measurement function required in the Newton iterations equations.

4.3.1 Evaluation of the Jacobian for the Newton Method

The critical step in the numerical implementation of the regularized Newton method in Eq. (5.48) is the computation of the Jacobian J_H at each iteration m. Such computation must be executed with a high level of accuracy to ensure the stability, fast convergence and computational efficiency of the proposed Newton algorithm. We compute J_H using the following characterization of the derivative:

Theorem 2. *Let $v_l(t_j) = \dfrac{\partial x}{\partial \theta_l}(t_j)$ be the derivative of the solution $\vec{x}$ of HDS* (3.15) *with respect to θ_l, at time t_j. Then we have:*

$$\begin{cases} \dfrac{\partial v_l}{\partial \theta}(t) = \dfrac{\partial A}{\partial x}(x,t)v_l + \dfrac{\partial A}{\partial \theta}(x,t) \\ \dfrac{\partial y}{\partial \theta}(t) = \dfrac{\partial H}{\partial x}(x,t)v_l + \dfrac{\partial H}{\partial \theta}(x,t) \\ \dfrac{\partial x}{\partial \theta}(t=0) = 0 \end{cases} \tag{4.49}$$

where: $\dfrac{\partial v_l}{\partial \theta}$ is calculated as:

$$
\begin{cases}
\dot{v}_{l1} &= v_{l2} \\
\dot{v}_{l2} &= -\theta_3 v_{l2} - \theta_4 v_{l1} + \delta_{l2} u(t) - \delta_{l3} x_2 - \delta_{l4}(x_1 - 1) \\
\dot{v}_{l3} &= \theta_5 \left[v_{l1} - \theta_1 x_3^{\theta_1 - 1} v_{l3} \right] + \delta_{5l}(x_1 - x_3^{\theta_1}) - \delta_{l1}\theta_5 x_3^{\theta_1} \ln x_3 \\
\dot{v}_{l4} &= \theta_5 \left[\dfrac{v_{l1}}{\theta_6} \left((1 - (1-\theta_6)^{1/x_1}) + \dfrac{(1-\theta_6)^{1/x_1} \ln(1-\theta_6)}{x_1} \right) - \right. \\
& \quad \left. x_3^{(\theta_1 - 1)} v_{l4} - (\theta_1 - 1) x_4 x_3^{(\theta_1 - 2)} v_{l3} \right] \\
& \quad + \theta_5 \left[\dfrac{\delta_{6l}}{\theta_6} \left((1-\theta_6)^{1/x_1 - 1} - \dfrac{x_1}{\theta_6}(1 - (1-\theta_6)^{1/x_1}) \right) - x_4 x_3^{(\theta_1 - 1)} \delta_{l1} \ln x_3 \right] \\
& \quad + \delta_{5l} \left(x_1 \dfrac{1 - (1-\theta_6)^{1/x_1}}{\theta_6} - x_4 x_3^{(\theta_1 - 1)} \right) \\
& \quad v_{l1}(0) = v_{l2}(0) = v_{l3}(0) = v_{l4}(0) = 0
\end{cases}
\tag{4.50}
$$

where, $\vec{v}_{li} = \dfrac{\partial x_i}{\partial \theta_l}$, for $i = 1, \cdots, 4$ and $l = 1, \cdots, n_p$, and,

$$
\begin{aligned}
\frac{\partial y}{\partial \theta}(t_j) = \frac{\partial H}{\partial \theta_l}(t_j) &= \delta_{7l} \left[7\theta_6(1 - x_{j4}) + 2(1 - \frac{x_{j4}}{x_{j3}}) + (1 - x_{j3})(2\theta_6 - 0.2) \right] \\
&+ \delta_{6l} \left[7\theta_7(1 - x_{j4}) + (1 - x_{j3}) 2\theta_7 \right] \\
&- v_{l4}\theta_7 \left[7\theta_6 + \frac{2}{x_{j3}} \right] + v_{l3}\theta_7 \left[\frac{2x_{j4}}{x_{j3}^2} - 2\theta_6 + 0.2 \right]
\end{aligned}
\tag{4.51}
$$

Note that the differentiability of $\vec{x}$ follows from the classical regularity results of the solution of a time evolution equation with respect to the coefficients of HDS (3.15). The proof of Theorem 2 is then a direct consequence of the differentiability of $\vec{x}$ and the use of the chain rule. Therefore, we can construct the Jacobian matrix $J_H(\theta^{(m)})(t_j) = \left[\dfrac{\partial H}{\partial \theta_l}(\theta^{(m)})(t_j) \right]$ for $j = 1, \ldots, M$, where M is the number of measurements, and $l = 1, \ldots, n_p$, where n_p is the number of parameters. Also, note that the IVP given by Eq. (4.50) is different from the IVP given by Eq. (3.15) only by extra terms on the right hand side.

Chapter 5

Parameter Estimation

The construction of reliable model has raised the challenging question of estimating the model parameters, hidden states and ultimately the neural activity. The first important attempt has been proposed by [20] using Volterra Kernel expansion to characterize the deterministic hemodynamic response. The bayesian framework was introduced by [13] where the restriction induced by the use of temporal basis was replaced by Gaussian priors on the parameters, the nonlinear dynamic equation was also approximated using a bilinear equation to facilitate the likelihood maximization. To account for physiological noise, [44] added a wiener process to the dynamics equation. He used a Local Linearization Filter (LLF) based on a truncated Ito-Taylor expansion of the dynamics equation to estimate the state and parameters of the balloon model and introduced a fixed number of radial basis functions to approximate the neural activity.

Similar filtering approaches were proposed by [10] (iterative extended Kalman filtering coupled with simplex search method), [29] (particle filtering), [37] (particle smoothing), [25] (Unscented Kalman filtering) and used to infer model states and parameters with more or less accuracy of the estimation and computational complexity. Some of the filtering techniques, namely the extended Kalman filtering and the particle filtering were compared to a variational Bayesian method called Dynamic Expectation Maximization (DEM), proposed by [18], which has shown better results in terms of robustness. However, it was shown in [23] that Cubature Kalman filter (CKF) [1] and its square root form outperforms the DEM.

The methods reported above used different strategies to add prior knowledge that makes the estimation problem well-posed. For example, [44] used radial basis functions to express the input while [23] supposed Gaussian priors for the parameters. Small prior variances are sought to overcome the identifiability issues of some parameters.

In this chapter we introduce a new algorithm, which employes two powerful tools, namely, the Cubature Kalman filtering (CKF) and a regularized Newton algorithm (RNA) to estimate the parameters and the state of the nonlinear dynamical system described in 3.1.3. This algorithm uses CKF to de-noise the state from a set of noisy measurements and RNA to estimate the parameters of the considered nonlinear system.

We begin this chapter by describing the CKF algorithm in §5.1. We then present the RNA algorithm in §5.2. §5.3 is devoted to the description of the proposed solution method-

ology.

5.1 Cubature Kalman Filtering Method (CKF)

5.1.1 Kalman Filtering Frame Work

Kalman filter also known as linear quadratic estimation (LQE) is an efficient recursive filter that estimates the internal state of a linear dynamical system from a series of noisy measurements. The Kalman filter has been the subject of extensive research and application. It has numerous applications in technology. A common application of this filter is for guidance, navigation and control of vehicles, particularly aircraft and spacecraft. Furthermore, the Kalman filter is a widely applied concept in time series analysis used in fields such as signal processing and econometrics.

The Kalman filter is a set of mathematical equations that provides an efficient recursive solution of the least-square method. The filter is very powerful in several aspects: it supports estimations of past, present and even future states, and it can do so even when the precise nature of the modeled system is unknown. Unlike most of the classical parameter estimation methods, the Kalman filter is a recursive estimator. At each time step the filter refines the previous estimate by incorporating in it new information from the model and from the output [32].

The Kalman filter works in two steps: first it estimates the process state and covariance at some time using information from the process only (prediction); then it employs a feedback from the noisy measurements to improve the first estimates (correction). As such, the equations for the Kalman filter fall into two groups: time update equations for the prediction step and measurement update equations for the correction step. The time update equations are responsible for propagating forward (in time) the current state and error covariance estimates to obtain the a priori estimates for the next time step. The measurement update equations are responsible for the feedback, i.e. for incorporating a new measurement into the a priori estimate to obtain an improved a posteriori estimate. After each time and measurement update pair, the process is repeated with the previous a posteriori estimates used to predict the new a priori estimates.

In order to see these ideas in a more rigorous mathematical framework, consider the following system:

$$\begin{cases} x_{t+1} = f(x_t, u_t) + v_t \\ y_{t+1} = h(x_{t+1}, u_{t+1}) + w_{t+1} \end{cases} \tag{5.1}$$

where $f : \mathbb{R}^{n_x} \times \mathbb{R}^{n_u} \to \mathbb{R}^{n_x}$ and $h : \mathbb{R}^{n_x} \times \mathbb{R}^{n_u} \to \mathbb{R}^{n_z}$ are some known functions; u_t is the known control input; y_t represents the measurement. The variable v_t, usually called the *process noise*, represents the amount of confidence we have in our model. The process noise is assumed to be a Gaussian random variable with zero mean and covariance Q[1], where Q is a positive definite matrix. The noise that affects the different components of the state is assumed to be uncorrelated, so that Q is diagonal. Larger entries in Q correspond to lower confidence in the accuracy of the model. The variable w_t is referred to as the *measurement noise*, and expresses the reliability of the measurements. The measurement noise is also assumed to be Gaussian with zero mean, and its covariance matrix will be denoted by R[2]. Again, R is assumed to be a positive definite, diagonal matrix, since the noise that affects different measurements is assumed to be uncorrelated. Note that while Q is usually chosen by the user in order to tell the filter how much the model should be trusted, R is fixed by the quality of the measurements. In other words, the statistics of the measurements noise are assumed to be known [32].

The key approximation to develop Bayesian filter theory under Gaussian domain is that the predictive density $p(x_{t+1}|D_t)$ and the filter likelihood density $p(y_{t+1}|D_{t+1})$ are both Gaussian, which eventually leads to a Gaussian posterior density $p(x_{t+1}|D_{t+1})$. $D_t = \{u_i, y_i\}_{i=0}^{t}$ represents the history of input-measurement pairs up to time t.

In the prediction step, the filter produces estimates of the current state variables, along with their uncertainties. In other words it calculates the mean $\hat{x}_{t+1|t}$ and the associated covariance $P_{t+1|t}$ of the Gaussian predictive density. We have

$$\hat{x}_{t+1|t} = \mathbb{E}[x_{t+1}|D_t] \tag{5.2}$$

where $\mathbb{E}$ is the statistical expectation operator. Eqs. (5.1) and (5.2) will then give:

$$\hat{x}_{t+1|t} = \mathbb{E}[f(x_t, u_t) + v_t|D_t]. \tag{5.3}$$

Since v_t is assume to be zero-mean and uncorrelated with the past measurements, we get

$$\begin{aligned} \hat{x}_{t+1|t} &= \mathbb{E}[f(x_t, u_t)|D_t] \\ &= \int_{\mathbb{R}^{n_x}} f(x_t, u_t) p(x_t|D_t) dx_t \\ &= \int_{\mathbb{R}^{n_x}} f(x_t, u_t) \times \mathcal{N}(x_t; \hat{x}_{t|t}, P_{t|t}) dx_t \end{aligned} \tag{5.4}$$

[1] $v_t \sim \mathcal{N}(0, Q)$
[2] $w_t \sim \mathcal{N}(0, R)$

Throughout what follows, $\mathcal{N}(x;\mu,\Sigma)$ is used as a conventional symbol for a Gaussian density of random variable x with mean value μ and covariance Σ.

Similarly, we obtain the associated error covariance as follows

$$\begin{aligned} P_{t+1|t} &= \mathbb{E}[(x_{t+1}-\hat{x}_{t+1|t})(x_{t+1}-\hat{x}_{t+1|t})^T|y_{1:t}] \\ &= \int_{\mathbb{R}^{n_x}} f(x_t,u_t)f^T(x_t,u_t)\times\mathcal{N}(x_t;\hat{x}_{t|t},P_{t|t})dx_t \\ &\quad -\hat{x}_{t+1|t}\hat{x}_{t+1|t}^T+Q. \end{aligned} \tag{5.5}$$

In the correction step first the predicted measurement $\hat{y}_{t+1|t}$ and its associated covariance $P_{yy,t+1|t}$ are calculated.

$$\begin{aligned} \hat{y}_{t+1|t} &= \mathbb{E}[y_{t+1}|D_t] \\ &= \mathbb{E}[h(x_{t+1},u_{t+1})+w_{t+1}|D_t] \end{aligned} \tag{5.6}$$

Again since w_t is assumed to be zero-mean and uncorrelated with the past measurements, we get

$$\begin{aligned} \hat{y}_{t+1|t} &= \mathbb{E}[h(x_{t+1},u_{t+1})|D_t] \\ &= \int_{\mathbb{R}^{n_x}} h(x_{t+1},u_{t+1})\times\mathcal{N}(x_{t+1};\hat{x}_{t+1|t},P_{t+1|t})dx_{t+1} \end{aligned} \tag{5.7}$$

and the associated covariance is

$$\begin{aligned} P_{yy,t+1|t} &= \mathbb{E}[(y_{t+1}-\hat{y}_{t+1|t})(y_{t+1}-\hat{y}_{t+1|t})^T] \\ &= \int_{\mathbb{R}^{n_x}} h(x_{t+1},u_{t+1})h^T(x_{t+1},u_{t+1})\times\mathcal{N}(x_{t+1};\hat{x}_{t+1|t},P_{t+1|t})dx_{t+1} \\ &\quad -\hat{y}_{t+1|t}\hat{y}_{t+1|t}^T+R \end{aligned} \tag{5.8}$$

Therefore, the conditional Gaussian density of the joint state and the measurement can be written as

$$p\left([x_{t+1}^T y_{t+1}^T]^T|D_t\right)=\mathcal{N}\left(\begin{pmatrix}\hat{x}_{t+1|t}\\ \hat{y}_{t+1|t}\end{pmatrix},\begin{pmatrix}P_{xx,t+1|t} & P_{xy,t+1|t}\\ P_{yx,t+1|t} & P_{yy,t+1|t}\end{pmatrix}\right) \tag{5.9}$$

Since, covariance matrices are symmetric, therefore $P_{yx,t+1|t}=P_{xy,t+1|t}^T$, and it is given

by

$$P_{xy,t+1|t} = \int_{\mathbb{R}^{n_x}} x_{t+1} h^T(x_{t+1}, u_{t+1}) \times \mathcal{N}(x_{t+1}; \hat{x}_{t+1|t}, P_{t+1|t}) dx_{t+1} - \hat{x}_{t+1|t} \hat{y}^T_{t+1|t} \quad (5.10)$$

Once the outcome of the next measurement (necessarily corrupted with some amount of error, including random noise) is observed, the estimates obtained in the previous step ($\hat{x}_{t+1|t}$ and $P_{t+1|t}$) are updated using a weighted average, with more weight being given to estimates with higher certainty. The updated mean of the posterior density will then be

$$\hat{x}_{t+1|t+1} = \hat{x}_{t+1|t} + W_{t+1}(\tilde{y}_{t+1} - \hat{y}_{t+1|t}) \quad (5.11)$$

and its associated covariance is

$$P_{xx,t+1|t+1} = P_{xx,t+1|t} + W_{t+1} P_{yy,t+1|t} W^T_{t+1} \quad (5.12)$$

where the term W_{t+1} in Eqs. (5.11) and (5.12) is called "Kalman gain", and is calculated in the least square sense to minimize the $P_{xx,t+1|t+1}$ [1]. Kalman gain is given by the following equation:

$$W_{t+1} = P_{xy,t+1|t} P^{-1}_{yy,t+1|t} \quad (5.13)$$

A wide variety of Kalman filters have now been developed, from Kalman's original formulation, now called the "Simple Kalman filter". In the original Kalman filter, one of the main assumptions is the linearity of the underlying dynamic model, but in reality most of the dynamical systems that are being studied are not linear but nonlinear. This have led to extending the original Kalman filter to the one that can work with the nonlinear systems.

Cubature Kalman filter (CKF) is a recursive, nonlinear and derivative-free filtering algorithm, developed under Kalman filtering frame work for high-dimensional nonlinear state estimation . CKF computes the first two moments (that is, mean and covariance) of all conditional densities using a highly efficient numerical integration method called radial cubature rules [24, 1]. Since it is derivative free, it smoothes the solution and makes it less sensitive to the measurement noise.

5.1.2 Gaussian Cubature Integrals

In calculating the first two momenta of the random variables in the prediction and correction steps, we encounter integrals of the form of a nonlinear function multiplied by the Gaussian density function. Here we describe a method based on the assumption that the domain of integration is symmetric and Gaussian.

CKF specifically employs the third-degree spherical-radial rule to approximate the integrals of the form 'nonlinear function $\times$ Gaussian density', numerically using a set of m equally weighted symmetric cubature points.

Consider the integral of the following form:

$$I(f) = \int_{\mathbb{R}^n} f(x) \exp(-x^T x)\, dx \tag{5.14}$$

where, f is a nonlinear function and random variable x is a zero mean random variable with covariance $\mathbf{I}$.

Theorem 3. *For the case where the random variable x has normal distribution with mean value μ and covariance Σ we have:*

$$\int_{\mathbb{R}^n} f(x)\mathcal{N}(x;\mu,\Sigma)dx = \frac{1}{\sqrt{\pi^n}} \int_{\mathbb{R}^n} f(\sqrt{2\Sigma}x + \mu) \exp(-x^T x)dx \tag{5.15}$$

Proof. Using the change of variables $x = \sqrt{2\Sigma}y + \mu$, the probability density function for multivariate normal random variable $x \sim \mathcal{N}(\mu, \Sigma)$ is as follows:

$$f_x(\mathbf{x}) = \frac{1}{\sqrt{(2\pi)^n|\Sigma|}} \exp(-\frac{1}{2}(\mathbf{x}-\mu)^T\Sigma^{-1}(\mathbf{x}-\mu)) \tag{5.16}$$

Since Σ is a positive definite matrix, we can factorize Σ to be $\Sigma = \sqrt{\Sigma}\sqrt{\Sigma}^T$. Therefore, Eq. (5.15) becomes,

$$\begin{aligned} &= \int_{\mathbb{R}^n} f(\sqrt{2\Sigma}y + \mu)\frac{1}{\sqrt{2\pi|\Sigma|}} \exp(-y^T y)|\sqrt{2\Sigma}|dy \\ &= \frac{1}{\sqrt{\pi^n}} \int_{\mathbb{R}^n} f(\sqrt{2\Sigma}x + \mu) \exp(-x^T x)dx \end{aligned} \tag{5.17}$$

Where, $\mathbf{x}, \mu \in \mathbb{R}^n$, $\Sigma \in \mathbb{R}^{n\times n}$, $|\Sigma|$ is the determinant of Σ. □

To solve the integral in Eq. (5.14), we first use the following change of variable to transform the integral into spherical-radial integration form:

$$\mathbf{x} = r\mathbf{y} \tag{5.18}$$

with,

$$\mathbf{y}^T\mathbf{y} = 1. \tag{5.19}$$

Therefore,

$$\mathbf{x}^T\mathbf{x} = r^2, \quad r \in [0, \infty) \tag{5.20}$$

Then, Eq. (5.14) can be rewritten in the spherical-radial coordinate system as

$$I(f) = \int_0^\infty \int_{U_n} f(r\mathbf{y}) r^{n-1} \exp(-r^2) d\sigma(\mathbf{y}) dr \tag{5.21}$$

where, U_n is the surface of the sphere defined by $U_n = \{\mathbf{y} \in \mathbb{R}^n | \mathbf{y}^T\mathbf{y} = 1\}$ and $\sigma(.)$ is the area element on U_n. Therefore we have:

The *Radial* integral,

$$I = \int_0^\infty S(r) r^{n-1} \exp(-r^2) dr \tag{5.22}$$

where $S(r)$ is defined by the *spherical integral* with the unit weighting function $w(y) = 1$

$$S(r) = \int_{U_n} f(r\mathbf{s}) d\sigma(\mathbf{s}) \tag{5.23}$$

We use a m_r-point *Gaussian quadrature* to solve the integral in (5.22). *Gaussian quadrature* rule is a numerical approximation of the definite integral of a function as a weighted sum of function values at specified points within the domain of integration. An n-point *Gaussian quadrature* rule is a quadrature rule which gives an exact result for polynomials of degree $2n - 1$ or less by a suitable choice of the points r_j, for $j = 1, \ldots, n$. Therefore, the integral in (5.22) can be approximated as

$$\int_0^\infty S(r) r^{n-1} \exp(-r^2) dr = \sum_{i=1}^{m_r} a_i f(r_i) \tag{5.24}$$

where, r_i are the quadrature points and a_i are the weights. We use a m_s-point spherical-radial cubature rule to solve the integral in (5.23):

$$\int_{U_n} f(r\mathbf{s}) d\sigma(\mathbf{s}) = \sum_{i=1}^{m_s} b_i f(r s_i) \tag{5.25}$$

Therefore,

From (5.24) and (5.25) we have a $(m_s \times m_r)$-point spherical-radial cubature rule to solve (5.14):

$$\int_{\mathbb{R}^n} f(x) \exp(-x^T x)\, dx \approx \sum_{i=1}^{m_s} \sum_{i=1}^{m_r} a_i b_i f(r_i s_i) \tag{5.26}$$

For a third-degree spherical-radial rule, $m_r = 1$ and $m_s = 2n$, we have a total of 2n cubature points. Therefore for a standard Gaussian weighted integral:

$$I_{\mathcal{N}}(f) = \int_{\mathbb{R}^n} f(x)\mathcal{N}(x; 0, I)dx \approx \sum_{i=1}^{m} \omega_i f(\xi_i) \tag{5.27}$$

with, $\{\xi_i, \omega_i\}_{i=1}^m$:

$$\begin{aligned} \xi_i &= \sqrt{\frac{m}{2}}\,[1]_i \\ \omega_i &= \frac{1}{m}, \quad i = 1, 2, \cdots, m = 2n_x \end{aligned} \tag{5.28}$$

where, ξ_i are the cubature points and ω_i are the weight functions. $[1]_i$ is the i-th element of $[1] \in \mathbb{R}^n$ which represents a completely fully symmetric set of points in $\mathbb{R}^n$ that can be obtained by permutation and changing the sign of the generator $(1, 0, 0, \cdots) \in \mathbb{R}^n$.

5.1.3 CKF Algorithm Summary

We can summarize the CKF algorithm as follows:

Step I: Time Update:

Assume that $\hat{x}_{t|t}$ and $P_{t|t}$ are the estimate for the state and its associated error covariance matrix at time t, respectively.

1. First step is to factorize the error covariance matrix $P_{t|t}$ associated with the state x_t. Since $P_{t|t}$ is positive definite and symmetric we use Cholesky factorization to get :

$$P_{t|t} = S_{t|t} S_{t|t}^T \tag{5.29}$$

2. Evaluate the cubature points. Since $x_t \sim (\hat{x}_{t|t}, P_{t|t})$, by Theorem 3 cubature points

are given by:

$$\mathbf{X}_{i,t|t} = S_{t|t}\xi_i + \hat{x}_{t|t}; \quad i = 1, 2, \cdots, m \tag{5.30}$$

where, ξ_i are given by Eq. (5.28).

3. Evaluate the process at the cubature points to obtain the propagated cubature points:

$$\mathbf{X}^*_{i,t+1|t} = f(\mathbf{X}_{i,t|t}, u_t); \quad i = 1, 2, \cdots, m \tag{5.31}$$

4. The average over the propagated cubature points will give us an estimate for the state at the next time step. We use this estimate as a prediction for the state. $\hat{x}_{t+1|t}$ denotes the estimate for the state given the measurements up to time t.

$$\hat{x}_{t+1|t} = \frac{1}{m}\sum_{i=1}^{m} \mathbf{X}^*_{i,t+1|t} \tag{5.32}$$

5. Then we calculate the predicted error covariance, associated with $\hat{x}_{t+1|t}$:

$$P_{t+1|t} = \frac{1}{m}\sum_{i=1}^{m} \mathbf{X}^*_{i,t+1|t}\mathbf{X}^{*T}_{i,t+1|t} - \hat{x}_{t+1|t}\hat{x}^T_{t+1|t} + Q \tag{5.33}$$

Step II: Measurement Update

6. Similar to step (1) we use the Cholesky factorization to factorize $P_{t+1|t}$ given by Eq. (5.33) to get:

$$P_{t+1|t} = S_{t+1|t}S^T_{t+1|t} \tag{5.34}$$

7. Then we evaluate the cubature points using the estimate for the state obtained by Eqs. (5.32) and (5.33):

$$\mathbf{X}_{i,t+1|t} = S_{t+1|t}\xi_i + \hat{x}_{t+1|t}; \quad i = 1, 2, \cdots, m \tag{5.35}$$

8. Then we evaluate the measurement function at the cubature points given by Eq. (5.34) to get the propagated cubature points:

$$\mathbf{Y}_{i,t+1|t} = h(\mathbf{X}_{i,t+1|t}, u_{t+1}), \quad i = 1, 2, \cdots, m \tag{5.36}$$

9. Then we calculate an estimate for the measurement at the next time step. We use

this value as a prediction for the measurement:

$$\hat{y}_{t+1|t} = \frac{1}{m}\sum_{i=1}^{m} \mathbf{Y}_{i,t+1|t} \tag{5.37}$$

10. Estimate the error covariance matrix associated with $\hat{y}_{t+1|t}$. In Kalman filtering framework this term is called *innovation* covariance matrix :

$$P_{yy,t+1|t} = \frac{1}{m}\sum_{i=1}^{m} \mathbf{Y}_{i,t+1|t}\mathbf{Y}_{i,t+1|t}^{T} - \hat{y}_{t+1|t}\hat{y}_{t+1|t}^{T} + R \tag{5.38}$$

11. The cross-covariance matrix is then given by:

$$P_{xy,t+1|t} = \frac{1}{m}\sum_{i=1}^{m} \mathbf{X}_{i,t+1|t}^{*}\mathbf{Y}_{i,t+1|t}^{T} - \hat{x}_{t+1|t}\hat{y}_{t+1|t}^{T} \tag{5.39}$$

12. Then we calculate the term called *Kalman gain*, which is calculated in the least squares sense to minimize the state error covariance matrix:

$$W_{t+1} = P_{xy,t+1|t}P_{yy,t+1|t}^{-1} \tag{5.40}$$

13. At this point, we can update the predicted state obtained in step (4). $\hat{x}_{t+1|t+1}$ denotes the estimate for the state given the measurements up to time $t+1$.

$$\hat{x}_{t+1|t+1} = \hat{x}_{t+1|t} + W_{t+1}(\tilde{y}_{t+1} - \hat{y}_{t+1|t}) \tag{5.41}$$

14. The updated corresponding error covariance matrix is also given by:

$$P_{t+1|t+1} = P_{t+1|t} - W_{t+1}P_{yy,t+1|t}W_{t+1}^{T} \tag{5.42}$$

Then we repeat steps (1)-(14) with $\hat{x}_{t+1|t+1}$, and $P_{t+1|t+1}$ obtained from Eqs. (5.41) and (5.42).

5.2 The Regularized Newton Algorithm (RNA)

In recent fMRI studies some inversion methods, such as Dynamic expectation Maximization (DEM), Cubature Kalman filter (CKF), Sequential Monte Carlo (SMC), Square root Cubature Kalman filter (SCKF) have been used. Among these methods, SCKF has

been shown to outperform DEM, EKF, CKF and SMC [24]. However, applying the mentioned methods requires some a priori knowledge about the parameters of the system. Also, these methods do not account for the noise on the initial states. In this study we propose the regularized Newton method that can estimate the parameters efficiently with no prior information or assumption about their initial values. Furthermore, we prove that the combination of iterative regularized Newton method and CKF can significantly improve the reconstructions even in the presence of noise on the initial state. So far there has been some ambiguity about the uniqueness of the parameters based on numerical studies, in this paper we provide an important result based on mathematical analysis that shows the value of the parameters are in fact unique.

Finding the biophysiological parameters corresponding to a given profile as stated in (3.18) is an inverse problem that falls into the category of parameter estimation problems. This problem is difficult to solve, specially from a numerical point of view, because it is nonlinear and ill-posed in the sense of Hadamard [22]. In order to overcome these difficulties, we use a regularized Newton method. The iterative Newton method addresses the nonlinear aspect of the problem, while the Tikhonov regularization procedure addresses its ill-posedness and restores the stability of the problem.

We model the measured data as:

$$y = H(\vec{x}, \vec{\theta}) + w \tag{5.43}$$

Therefore, the problem of finding the set of parameters $\vec{\theta}$ that best describe the measured data y can be formulated as a minimization problem:

Given a measured BOLD signal $\tilde{y} = (\tilde{y}^0, \tilde{y}^1, \ldots, \tilde{y}^M)$, find admissible $\vec{\theta}$ such that:

$$\vec{\theta} = \operatorname{argmin}_{\theta} \left\| H(\vec{x}, \vec{\theta}) - \tilde{y} \right\|_2 \tag{5.44}$$

Solving the nonlinear equation (5.44) by the classical Newton method requires solving the following linearized system at each iteration m. Let $y^{(m)} = H^{(m)}(\vec{x}, \vec{\theta})$,

$$J_H^{(m)} \delta\vec{\theta}^{(m)} = \tilde{y} - y^{(m)} \tag{5.45}$$

and then we update $\vec{\theta}$

$$\vec{\theta}^{(m+1)} = \vec{\theta}^{(m)} + \delta\vec{\theta}^{(m)} \tag{5.46}$$

Here $J_H^{(m)} \delta\vec{\theta}^{(m)}(t_j) = \left[\frac{\partial H}{\partial \theta_l}(t_j) \right]$ is the Jacobian of the operator H. $J_H^{(m)} \delta\vec{\theta}^{(m)}$ is a $(M \times 7)$

matrix. The l^{th} column of J is the derivative of H with respect to θ_l at iteration m. In practice, the linear system (5.45) is overdetermined, hence we solve this system in the least squares sense. This means at each iteration m, we compute the $\delta\vec{\theta}$ as the solution of the normal equation:

$$J_H^{T(m)} J_H^{(m)} \delta\vec{\theta}^{(m)} = J_H^{T(m)} (\tilde{y} - y^{(m)}) \tag{5.47}$$

Also, note that the linear system (5.47) is severely ill-conditioned. Therefore, to address this issue we propose using the classical Tikhonov regularization procedure. That is we solve the following system at each iteration m:

$$(J_H^{T(m)} J_H^{(m)} + \alpha I)\delta\vec{\theta}^{(m)} = J_H^{T(m)} b \tag{5.48}$$

where,

$$b = \tilde{y} - y^{(m)}, \tag{5.49}$$

and the positive real number α represents the Tikhonov regularization parameter.

5.3 The Proposed Solution Methodology (RNA-CKF)

We propose a method which combines the two algorithms described in §5.1 and §5.2 to address the issues and limitations faced by using each one of these algorithms by itself. Since the system of interest is a nonlinear system, in the sense that both states and parameters of the system appear in the nonlinear way in the system, we need to use a method to address these nonlinearities. Also, the problem of identifying the parameters of this system is an ill-posed problem and therefore unstable, we designed this proposed algorithm which we refer to as RNA-CKF, in such a way to address all these difficulties. The Newton method addresses the nonlinearity of the system, while the regularization step addresses the instability of the problem. Moreover, CKF has been embedded in this algorithm to deal with the noise on the measurements and de-noise the states.

5.3.1 The algorithm

The RNA-CKF algorithm can be summarized as follows:

- **Step 0 (Initialization).** We start the algorithm with the initial data:

$$\vec{\theta}^{(m)} = \begin{bmatrix} \theta_1^{(m)} \\ \vdots \\ \theta_{n_p}^{(m)} \end{bmatrix}, \vec{\tilde{y}} = \begin{bmatrix} y_1 \\ \vdots \\ y_M \end{bmatrix}, \vec{x}_0^{(m)} = \vec{x}^{(m)}(0), \mathbf{P}^{(m)}, \mathbf{Q}, \mathbf{R} \tag{5.50}$$

where,

- $\vec{\theta}^{(m)}$ is the value of the parameters at iteration m.
- $\vec{\tilde{y}}$ is the measured BOLD signal that is tainted with noise.
- $\vec{x}_0^{(m)}$ is the initial value of the state variables at iteration m and at time ($t = 0$).

- **Step 1 (At iteration m).** We assume that we have computed the biophysiological parameters $\vec{\theta}^{(i)} = (\theta_1^{(i)}, \theta_2^{(i)}, \ldots, \theta_7^{(i)})$; for $0 \leq i \leq m$. Then, using $\vec{\theta}^{(m)}$ we apply CKF to a get the out put that is the BOLD signal, $\vec{y}^{(m)}$. Since CKF is a de-noising filter which de-noises the state while producing the output. This step requires $M \times 2n_x$ times solving the HDS.

- **Stopping criteria.** At each iteration after producing an output, we check the stopping criteria:

$$\|\vec{\tilde{y}} - \vec{y}^{(m)}\|_2 < \epsilon \tag{5.51}$$

  If the inequality (5.51) holds, we stop the algorithm, and take $\vec{\theta}^{(m)}$ as the estimated values of the parameters and $\vec{y}^{(m)}$ is the reconstructed BOLD signal. Otherwise, we go to the next step.

- **Step 2 (Update $\vec{\theta}^{(m+1)}$).** At this step, we evaluate $\delta\theta^{(m)}$ by solving the (7×7) system given in Eq. (5.47), and update the parameters to use in the next iteration. We use RNA to calculate $\vec{\delta\theta}^{(m)}$. The calculation is as follows:

  - **Step 2-1:** First we find $\vec{v}_{li} = \dfrac{\partial x_i}{\partial \theta_l}$, solution of the HDS, for $i = 1, \cdots, 4$ and $l = 1, \cdots, n_p$ (n_p being the number of parameters). We solve HDS using Runge-Kutta order 4 with the initial condition:

$$\vec{\theta} = \vec{\theta}^{(m)}, \quad \vec{x} = \vec{x}^{(m)} \tag{5.52}$$

  - **Step 2-2:** Then, we calculate $J_H(\theta_l^{(m)})(t_j)$ for $l = 1, \cdots, n_p$ and $j = 1, \cdots, M$, as described in Theorem 2. Once we build the Jacobian matrix, J_H. For $\vec{\theta} = \vec{\theta}^{(m)}$, and $\vec{x}_j = \vec{x}^{(m)}(t_j)$.
  - **Step 2-3:** Next, we get the Taylor expansion of the measurement equation, Eq. (3.17), that is:

$$\vec{\tilde{y}} = \vec{y}^{(m)} + J_H^{(m)} \vec{\delta\theta}^{(m)} \tag{5.53}$$

where, m is the number of iterations. Let,

$$\vec{\tilde{y}} - \vec{y}^{(m)} = b \tag{5.54}$$

Using the regularization parameter α we have:

$$(J_H^{T(m)} J_H^{(m)} + \alpha I)\vec{\delta\theta}^{(m)} = J_H^{T(m)} b \tag{5.55}$$

– **Step 2-4:** Once we calculate $\vec{\delta\theta}^{(m)}$ we update the parameters as follows:

$$\vec{\theta}^{(m+1)} = \vec{\theta}^{(m)} + \vec{\delta\theta}^{(m)} \tag{5.56}$$

- **Step 3:** Now using $\vec{\theta}^{(m+1)}$ and $\vec{x}^{(m+1)}$ we repeat the steps (1) and (2) to get a new BOLD signal.

5.3.2 Schematic Diagram

This algorithm can be summarized in the following diagram

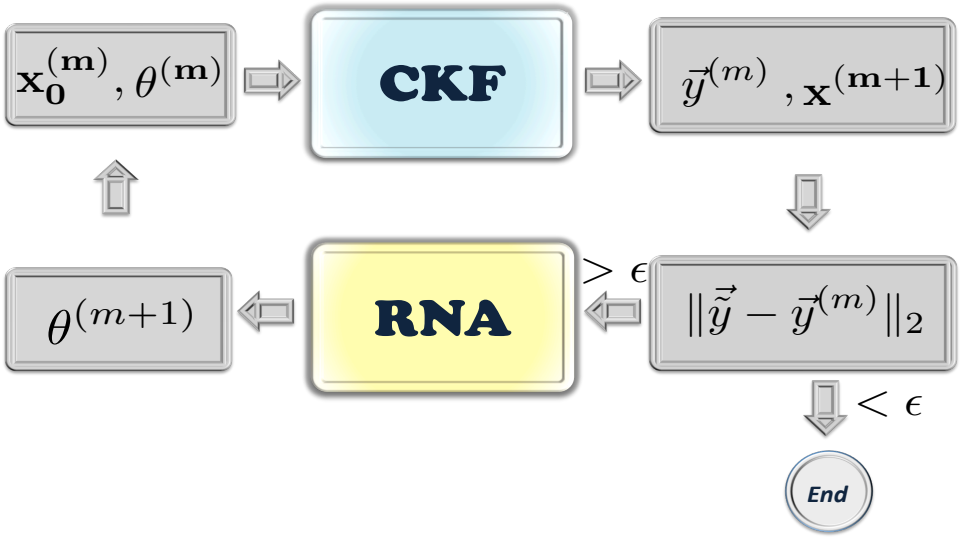

Figure 5.1: RNA-CKF schematic diagram.

Chapter 6

Performance Assessment: Illustrative Results

We demonstrate in this chapter, the performance of the proposed solution methodology for calibrating the hemodynamical model of brain responses. To this end, we first present the results of a numerical investigation that illustrates the sensitivity of the response to the change in the parameters. Then, we present the calibration results obtained by performing two categories of experiments: numerical simulations using synthetic data, and numerical simulations using real, *in vivo* data received from Nationwide Childrens Hospital, Columbus, OH.

6.1 Sensitivity Analysis: A Numerical Study

Similarly to the [10], we numerically investigate in this section the dependance of the response to the changes in the parameters of the system. We denote θ_i to be the parameter we are investigating its sensitivity and $\tilde{\theta}$ be the rest of parameters ($\theta = \{\theta_i, \tilde{\theta}\}$), and $J = \dfrac{\partial \mathcal{F}}{\partial \theta}(x, u, \theta)$ be the Jacobian and J_i be the i^{th} column of the Jacobian matrix and $\tilde{J}$ the matrix consisting of the remaining columns. Then for a small parameter change $d\theta$ we have:

$$\mathcal{F}(u, \theta + d\theta) = \mathcal{F}(u, \theta) + Jd\theta = \mathcal{F}(u, \theta) + J_i d\theta_i + \tilde{J}\tilde{\theta} \tag{6.1}$$

Note that, for a small change $d\theta_i$ of θ_i, f varies by $J_i\theta_i$. However, if J_i is not orthogonal to the other Jacobian components $\tilde{J}$, part of this variation can be compensated by a pseudo-inverse of $\tilde{J}$. Then we have:

$$\min_{d\tilde{\theta}} \|\mathcal{F}(u, \theta + d\theta) - \mathcal{F}(u, \theta)\| = \|(I - \tilde{J}\tilde{J}_H^+)J_i d\theta_i\| = \pi_i |d\theta_i|, \tag{6.2}$$

where

$$\pi_i = \|(I - \tilde{J}\tilde{J}_H^+)J_i\| = \sqrt{J_i^T (I - \tilde{J}\tilde{J}_H^+)J_i} \tag{6.3}$$

π_i indicates how much the system output is sensitive to variations of parameter θ_i. Therefore, the bigger π_i, the more identifiable θ_i is.

We calculate π_i for $i = 1, 2, \ldots, 7$, for the parameter values given in [5] that are listed in Table 6.1.

In addition, we investigated the identifiability of the parameters in the presence of measurement noise. As can be noted, increasing the noise on the measurements, makes

Parameters	Values	π_i
θ_1	$(.34)^{-1}$	9.43×10^{-4}
θ_2	.54	1.07×10^{-2}
θ_3	.65	5.16×10^{-2}
θ_4	.38	4.31×10^{-2}
θ_5	.98	3.61×10^{-3}
θ_6	.32	5.15×10^{-3}
θ_7	.04	2.33×10^{-1}

Table 6.1: Sensitivity level for θ_i

it harder to identify the parameters, whereas in the no noise case, we can almost exactly identify each parameter, fixing the others. Figure 6.1 shows the sensitivity of the model output to the change in parameters $\theta_1, \theta_2, \ldots, \theta_7$ when the parameter value varies from 0 to 1 for measurement noise ranging from 0% to 30%.

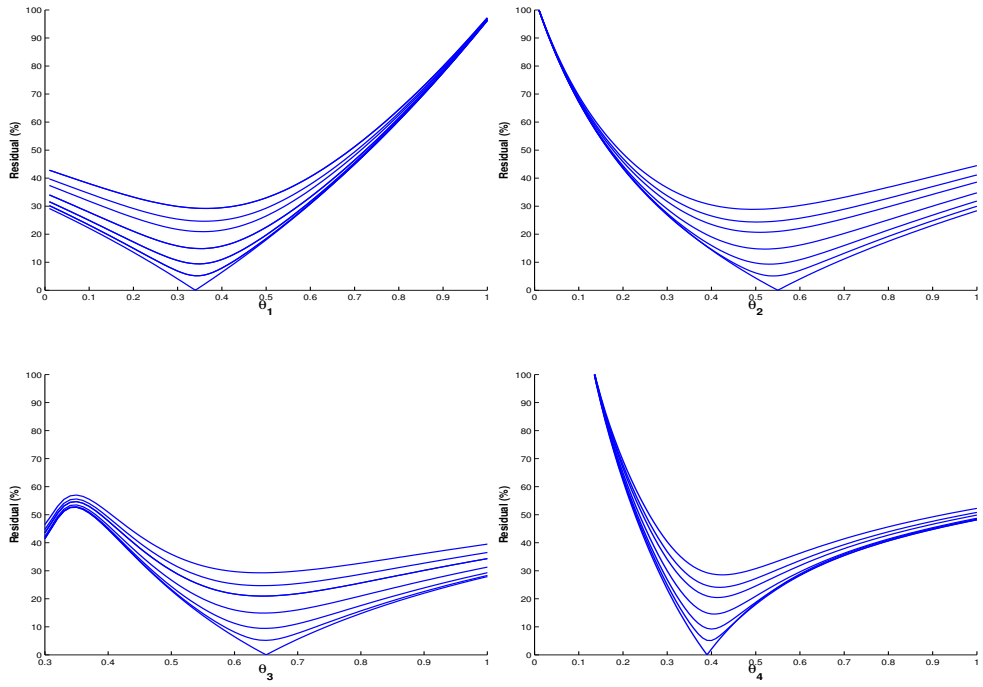

From the numerical experiments and the above sensitivity analysis we conclude that, in order to achieve the unique values of the parameters in the numerical experiments we need to work with high quality signal, where the signal to noise ratio (SNR) is high [10].

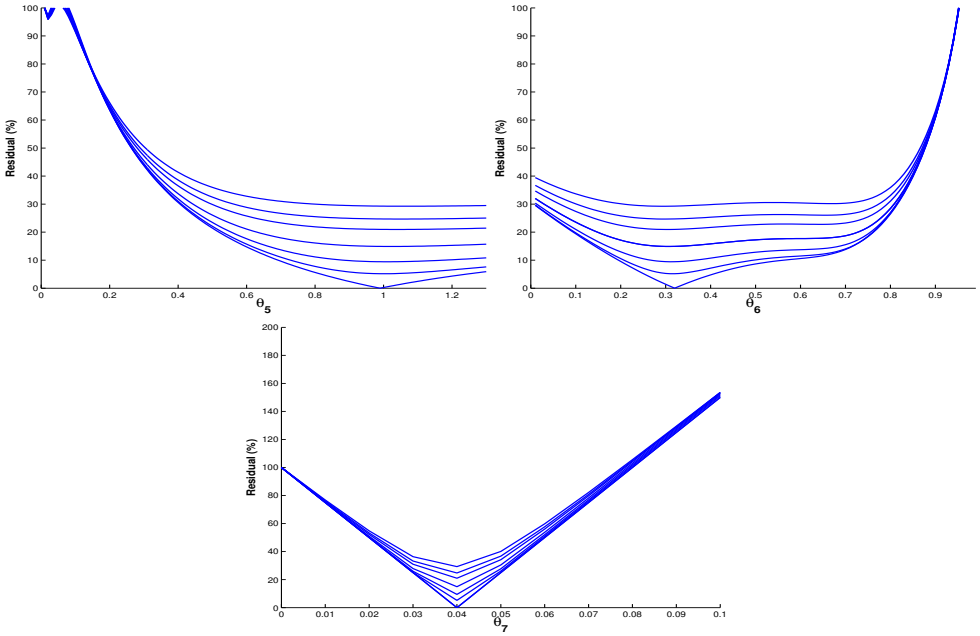

Figure 6.1: Residul on BOLD signal in the presence of 0%, 5%, 10%, 15%, 20%, 25%, 30% white noise on the measurements when parameters $\theta_1, \theta_2, \ldots, \theta_7$ vary from 0 to 1.

6.2 Parameter Estimation Using Synthetic Data

In this section, we present results of numerical experiments using synthetic data. Two sets of experiments have been performed. The first set has been particularly done to replicate the result in [24] and the second set has been done to mimic the real data. In each experiment, we solved the HDS using Runge-Kutta order 4 to generate a synthetic BOLD signal y. We must point out that the solver used to generate the synthetic data was different from the one which was used in the inversion algorithm, in order to avoid the so-called "inverse crime" [9].

6.2.1 Experiments With A Gaussian Control Input

In this section we used a Gaussian input given by Eq. (4.1) with $\mu = 25, \sigma = 6, t_f = 60\,s, \Delta t = 1\,s$ and the parameters listed in Table 6.2 to generate the synthetic BOLD signal. Figure 6.2 illustrates the noise-free generated BOLD signal with the Gaussian control input. Since in practice the given data is tainted with noise we added $1\% - 30\%$ white noise to the obtained signal. In practice measurements with 30% noise can be considered as highly noisy data, hence this simulations are performed in extreme situations. Also, to

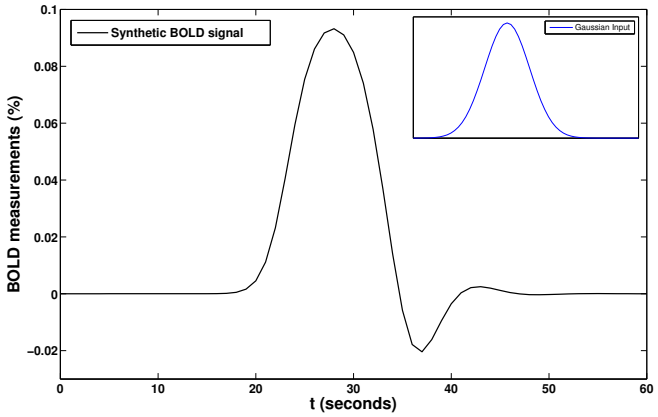

Figure 6.2: Synthetic BOLD signal corresponding to the Gaussian control input.

account for the possible noise on the initial state, we considered 5% white noise on $\vec{x}_0$. For the initial set of parameters, we chose a blind guess of $\vec{\theta} = [.5]$ in all the experiments.

Parameter	θ_1	θ_2	θ_3	θ_4	θ_5	θ_6	θ_7
Initial guess	$(.5)^{-1}$	.5	.5	.5	.5	.5	.5
Target	$(.34)^{-1}$	.54	.65	.38	.98	.32	.04

Table 6.2: Initial guess and target parameters for synthetic data generation with Gaussian input.

I. Comparison with CKF: We then compared the performance of the proposed algorithm RNA-CKF with CKF. As the results from [24] also suggest, CKF performs well when there is a priori knowledge about the initial value of the parameters available. However, in the case with blind initial guess CKF fails to provide a satisfactory reconstruction. However, RNA-CKF gives a good reconstruction for the BODL signal and the parameters and absolutely outperforms CKF with different level of noise on the measurements and the absence of a priori knowledge about the parameters (see Figure 6.3). It can also be observed that RNA-CKF reaches the level of noise on the measurement in all the experiments, while CKF fails (see Figure 6.6).

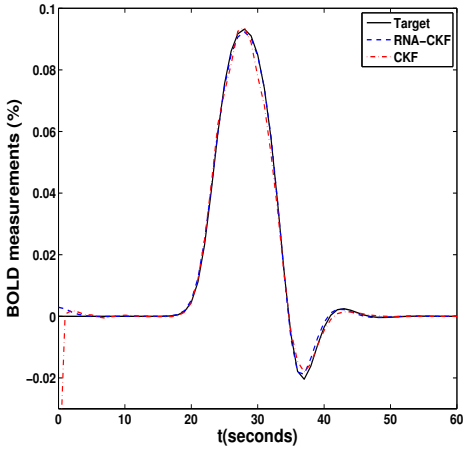

(a) 1% noise level

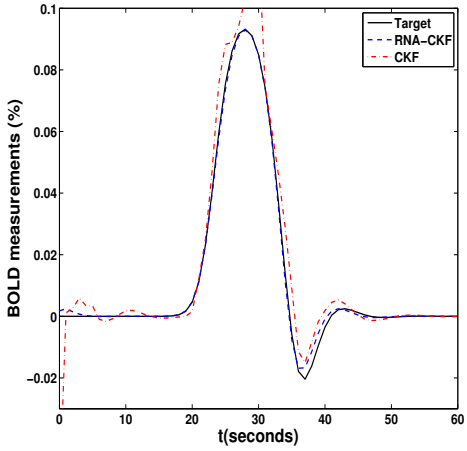

(b) 10% noise level

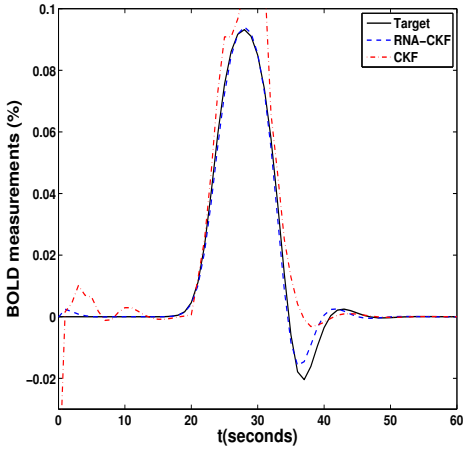

(c) 20% noise level

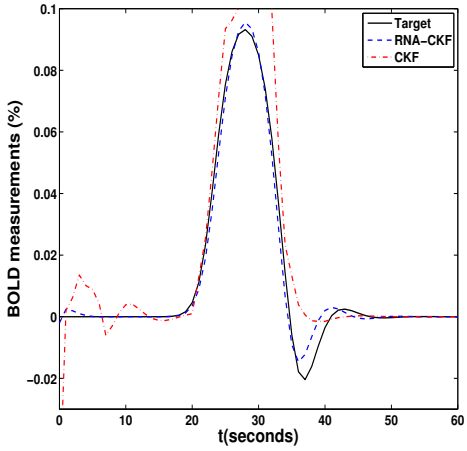

(d) 30% noise level

Figure 6.3: Target BOLD signal (Solid-black). Reconstructed BOLD signal using CKF algorithm (dashed-red) and RNA-CKF (dashed-blue), with 1%,10%,20%,30% white noise on the measurements.

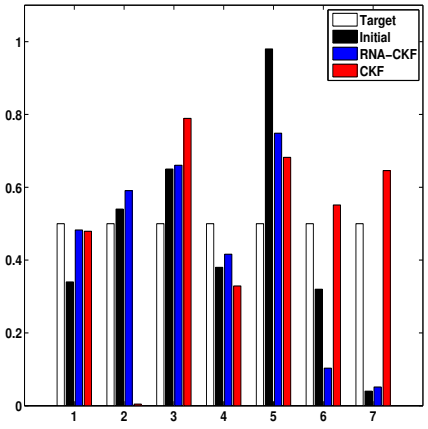

(a) 1% noise level

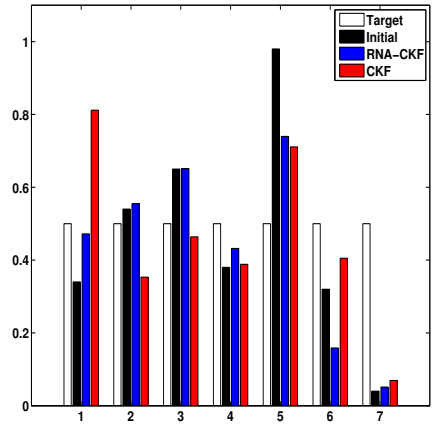

(b) 10% noise level

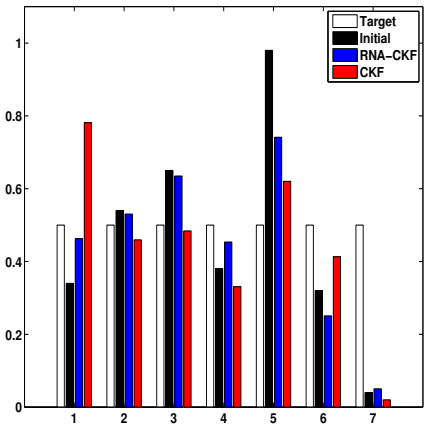

(c) 20% noise level

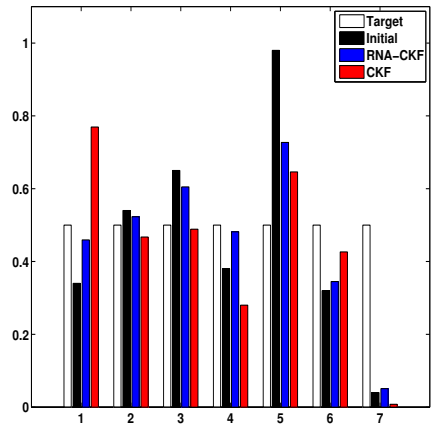

(d) 30% noise level

Figure 6.4: Target parameters (black). Initial parameters values (white). Reconstructed parameters using CKF algorithm (red) and RNA-CKF (blue), with 1%,10%,20%,30% white noise on the measurements.

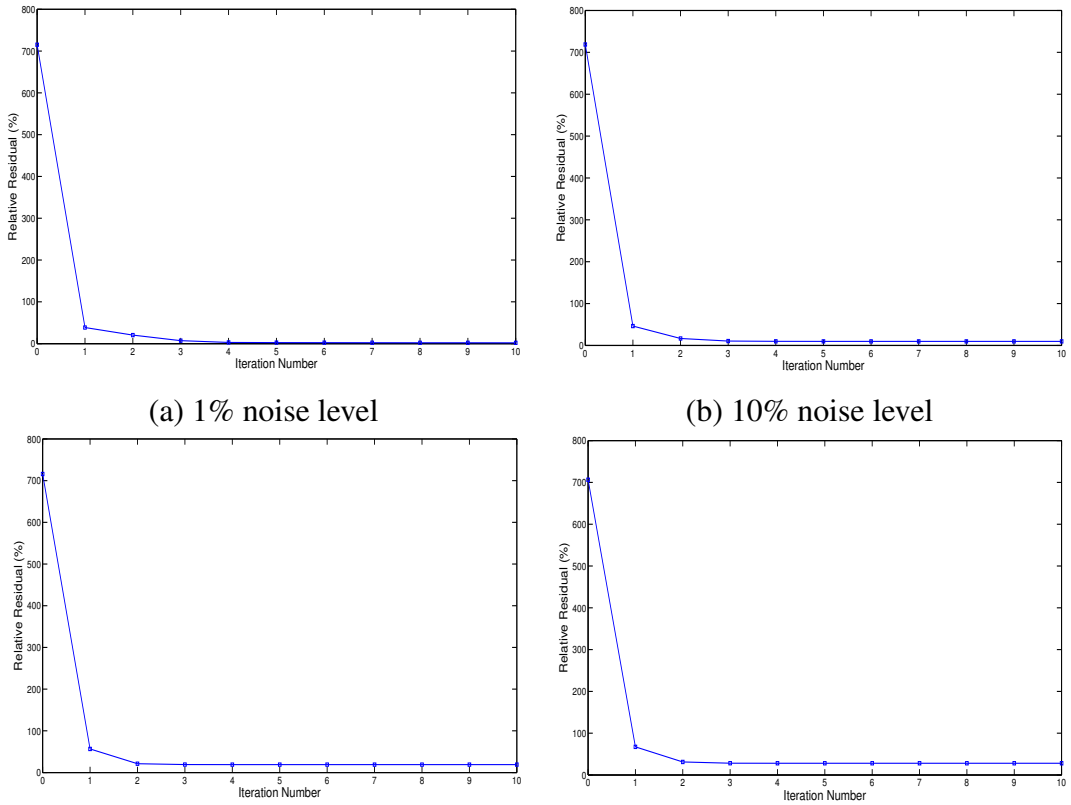

(a) 1% noise level

(b) 10% noise level

(c) 20% noise level

(d) 30% noise level

Figure 6.5: RNA-CKF convergence history for 1%,10%,20%,30% white noise on the measurements.

II. Comparison with RNA: In the next set of simulations we study the sensitivity of the proposed inversion algorithm RNA-CKF to the noise on the initial state and compare it to the result obtained from applying RNA. We considered $1\%, 10\%, 20\%, 30\%$ white noise on the initial state $\vec{x}_0$ while there is 30% white noise on the measurements. It is observed that both method provide fairly good reconstruction for the parameters. However, the reconstructed BOLD signal from RNA shows an initial increase in the signal, which indicates brain activity at the time when the stimulus has not been applied. On the other hand, the reconstructed BOLD signal from RNA-CKF algorithm provides a physiologically reliable output.

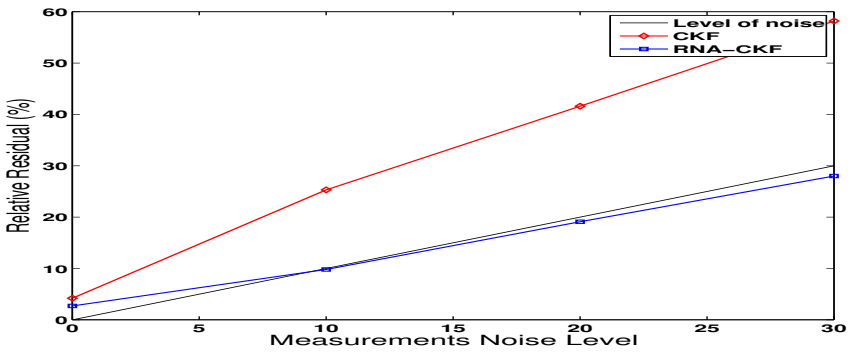

Figure 6.6: Comparing relative error on the computed BOLD signal using CKF and RNA-CKF, for 1%,10%,20%,30% white noise on measurements.

6.2.2 Experiments With A Square Control Input

In this section we illustrate the result we obtained by employing a more realistic control input to mimic the real data. We used an *On-Off* input given by Eq. (4.2) with $t_1 = 7\,s, t_2 = 37\,s, t_f = 72\,s, \Delta t = 3\,s$ and the parameters $\vec{\theta}$ listed in Table 6.3 to generate the synthetic BOLD signal. Figure 6.10 shows the noise-free generated synthetic BOLD signal. Since the real data seems to be tainted with 5%-7% noise, we added $0\%, 5\%, 7\%, 10\%$ white noise to these measurements to validate the performance of the proposed algorithm in the presence of noise on the data. Figure 6.12 shows the reconstructed BOLD signal using RNA-CKF algorithm. It can be observed that RNA-CKF provides excellent reconstruction for the BOLD signal and the parameters without any a priori knowledge about the parameters and in the presence of high level measurement noise. We ran the algorithm using the regularization parameter $\alpha = 15$.

Parameter	θ_1	θ_2	θ_3	θ_4	θ_5	θ_6	θ_7
Initial guess	$(.5)^{-1}$	.5	.5	.5	.5	.5	.5
Target	$(.45)^{-1}$	.6	.4	.15	.4	.3	1.05

Table 6.3: Initial guess and target parameters for synthetic data generation with square input.

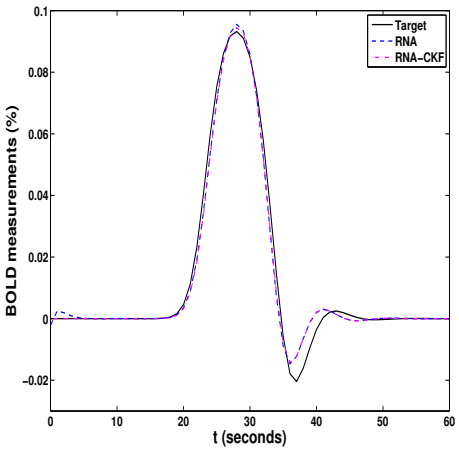

(a) 5% noise level

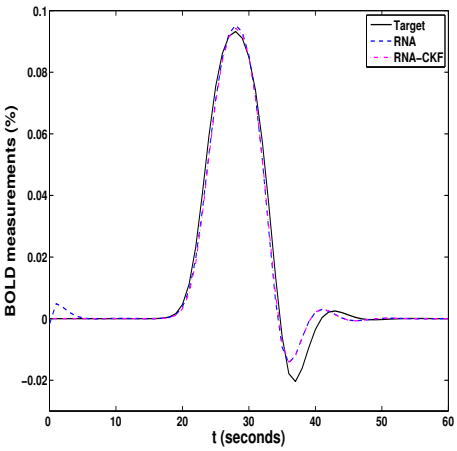

(b) 10% noise level

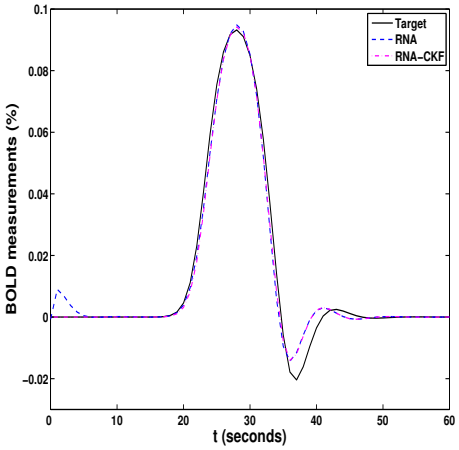

(c) 20% noise level

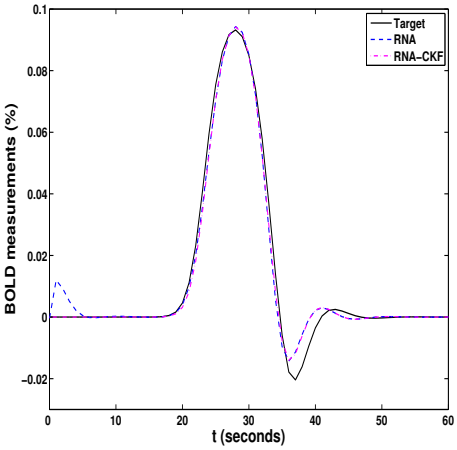

(d) 30% noise level

Figure 6.7: Target BOLD signal (solid-black). Reconstructed BOLD signal using RNA (dashed-blue) and RNA-CKF (dashed-magenta), with 5%,10%,20%,30% white noise on the initial state $\vec{x}_0$.

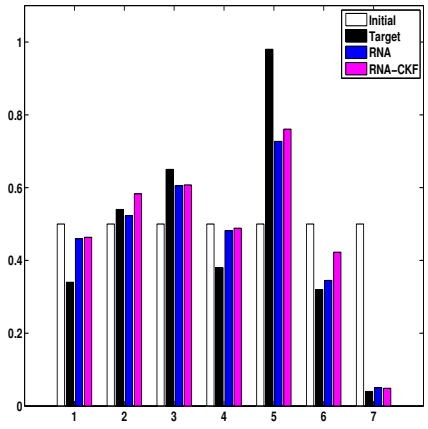

(a) 5% noise level

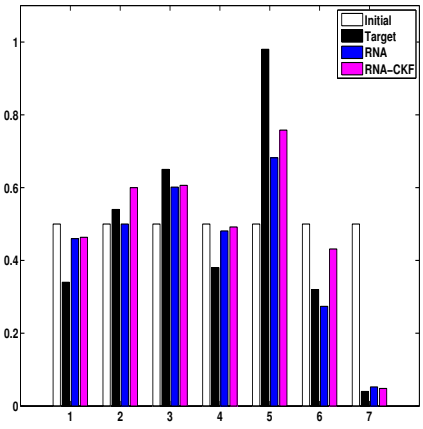

(b) 10% noise level

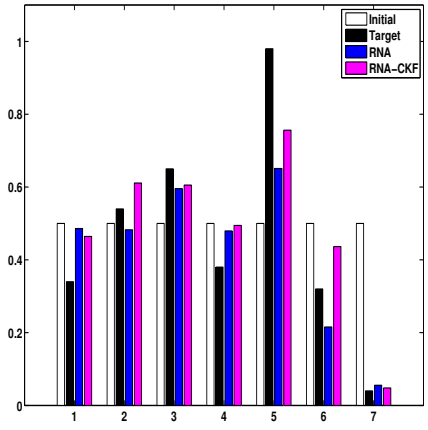

(c) 20% noise level

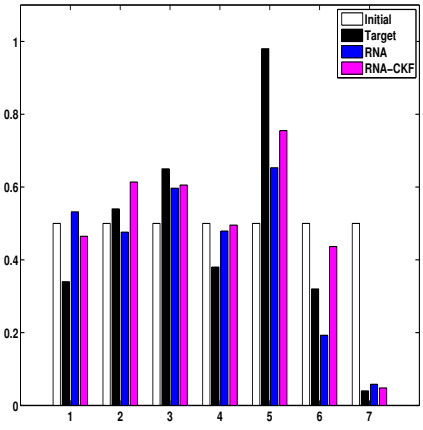

(d) 30% noise level

Figure 6.8: Target parameters (black). Initial parameters values (white). Reconstructed parameters using RNA (blue) and RNA-CKF (magenta), with 5%,10%,20%,30% white noise on the initial state $\vec{x}_0$.

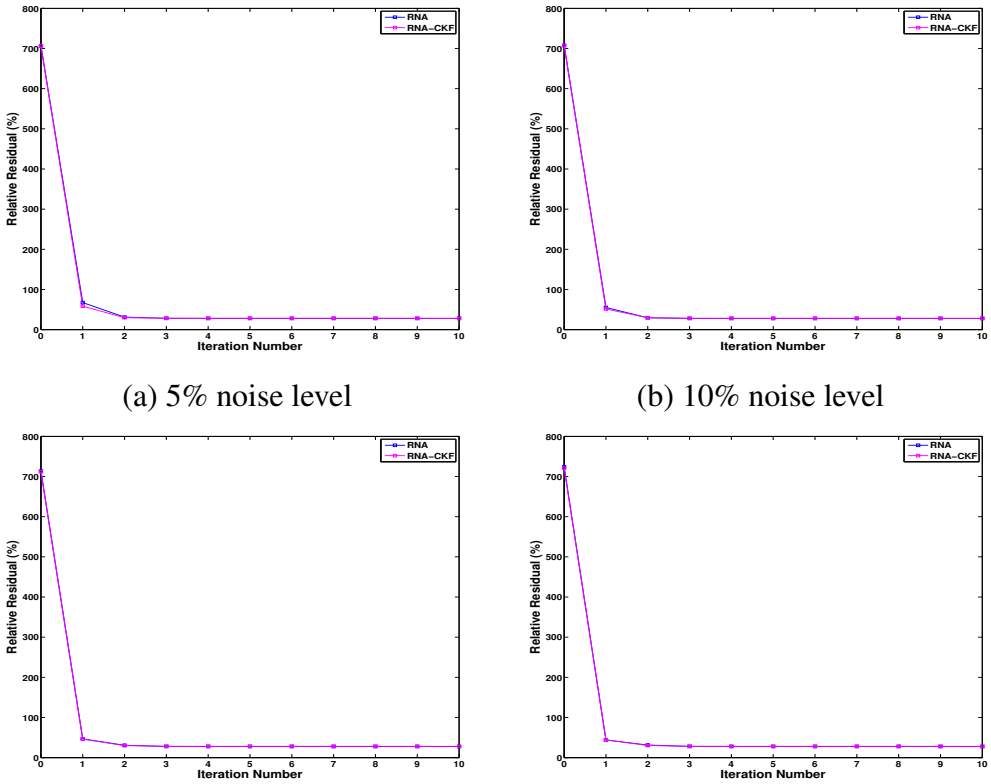

(a) 5% noise level

(b) 10% noise level

(c) 20% noise level

(d) 30% noise level

Figure 6.9: Convergence history for RNA (blue) and RNA-CKF (magenta) with 5%,10%,20%,30% white noise on the initial state $\vec{x}_0$.

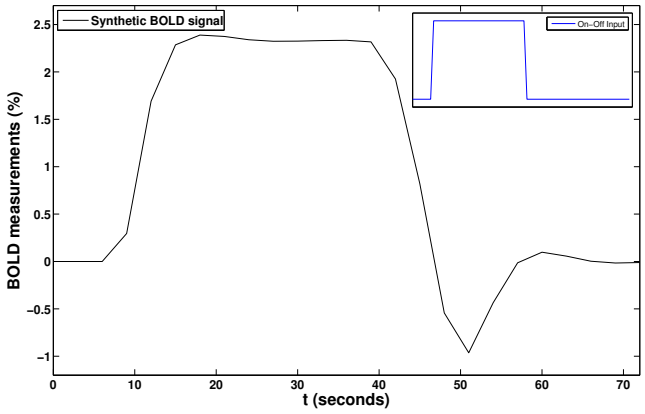

Figure 6.10: Synthetic BOLD signal corresponding to the *On-Off* control input.

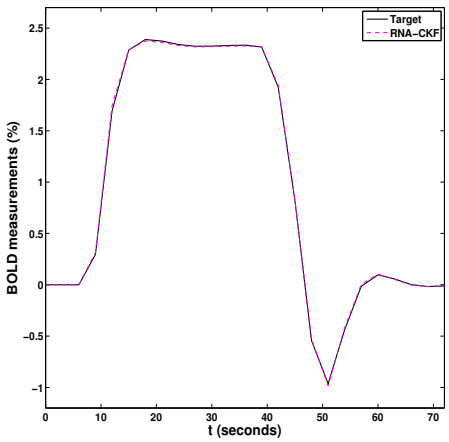

(a) 0% noise level

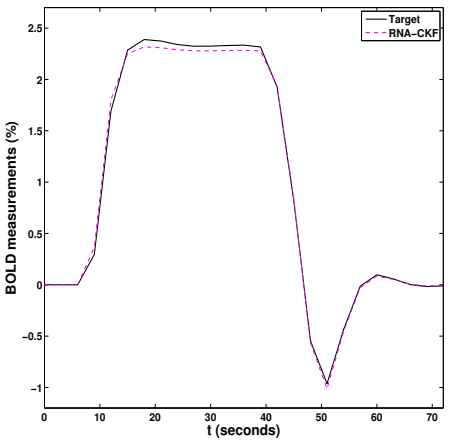

(b) 5% noise level

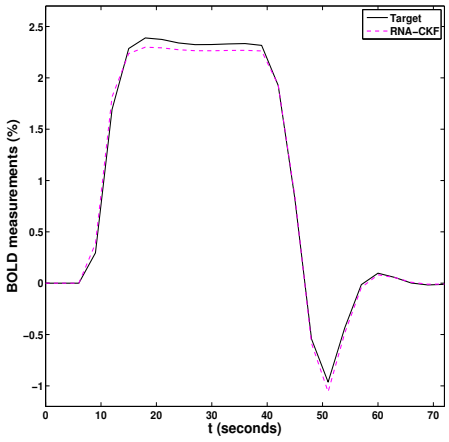

(c) 7% noise level

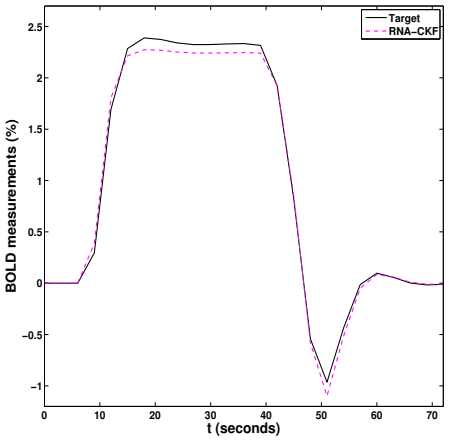

(d) 10% noise level

Figure 6.11: Reconstructed BOLD signal using inversion algorithm RNA-CKF and synthetic data, with 0%,5%,7%,10% white noise on the measurements and no additional noise on the initial state $\vec{x}_0$. The regularization parameter $\alpha = 18$.

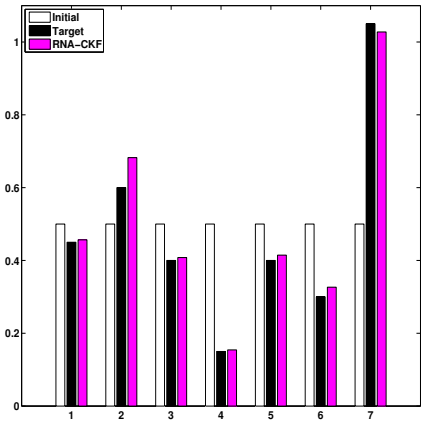

(a) 0% noise level

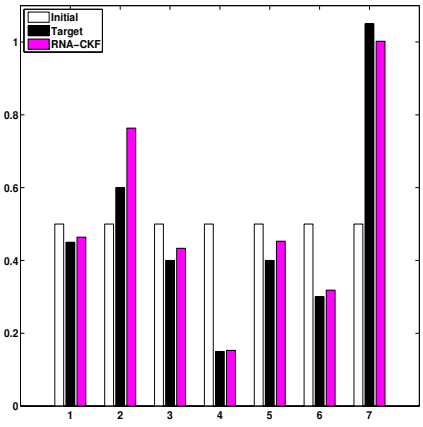

(b) 5% noise level

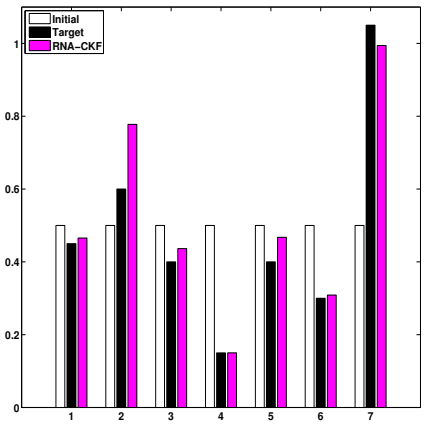

(c) 7% noise level

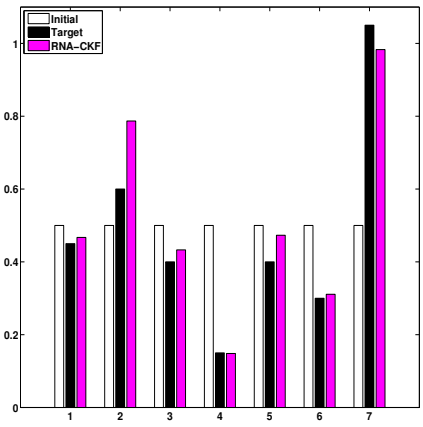

(d) 10% noise level

Figure 6.12: Reconstructed parameters using inversion algorithm RNA-CKF and synthetic data, with 0%,5%,7%,10% white noise on the measurements and the regularization parameter $\alpha = 18$ and no additional noise on the initial state $\vec{x}_0$.

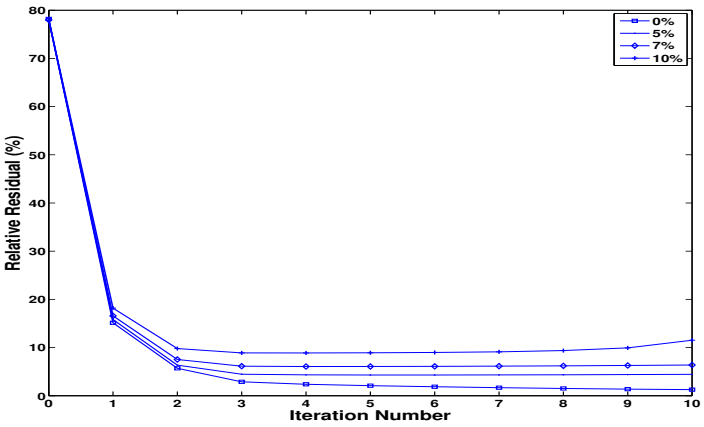

Figure 6.13: Convergence history for RNA-CKF with no noise on $\vec{x}_0$ and 0%,5%,7%,10% white noise on the measurements.

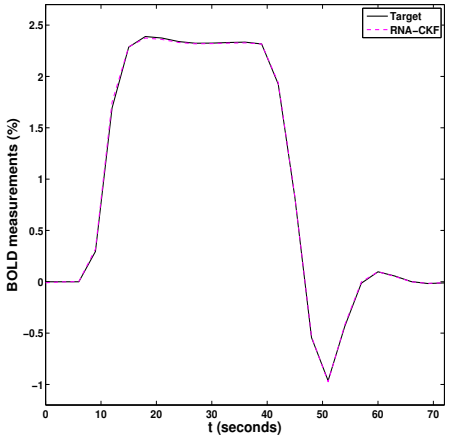

(a) 0% noise level

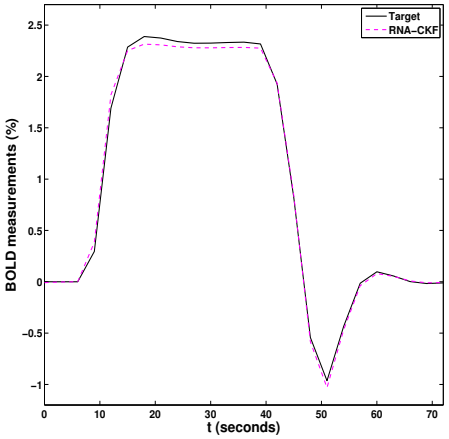

(b) 5% noise level

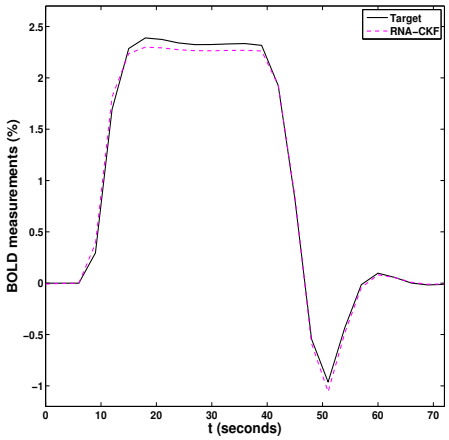

(c) 7% noise level

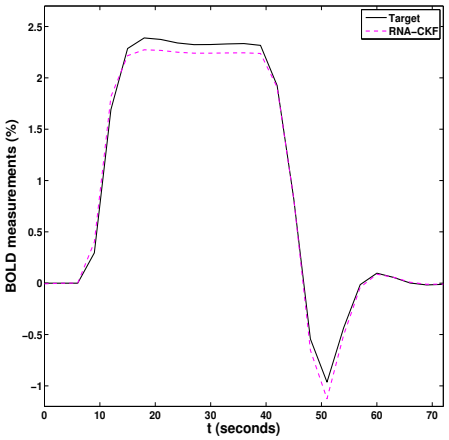

(d) 10% noise level

Figure 6.14: Reconstructed BOLD signal using inversion algorithm RNA-CKF and synthetic data, with 0%,5%,7%,10% white noise on the measurements and the regularization parameter $\alpha = 18$ and 5% noise on the initial state $\vec{x}_0$.

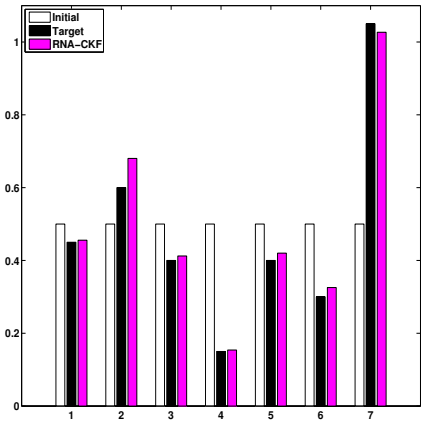

(a) 0% noise level

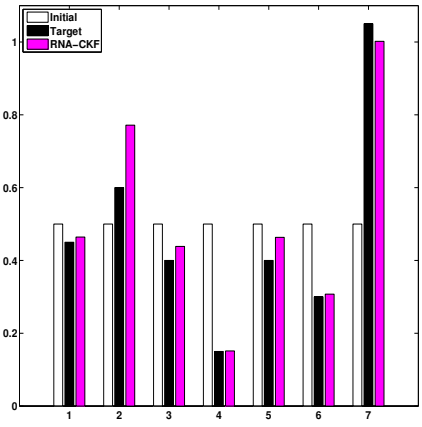

(b) 5% noise level

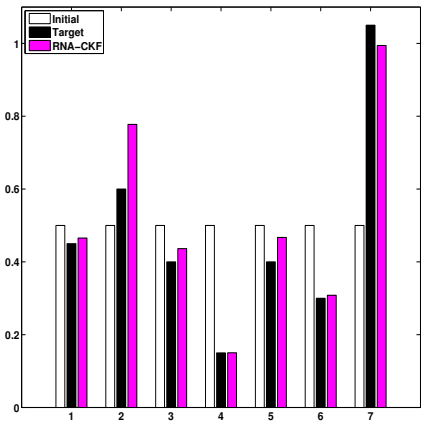

(c) 7% noise level

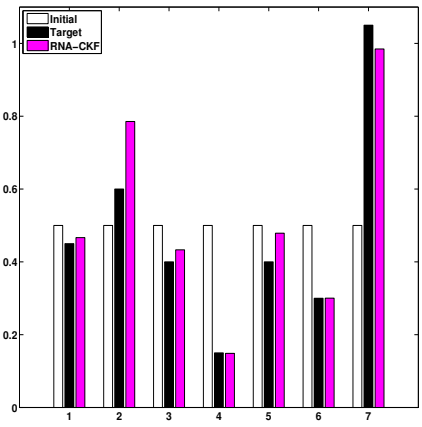

(d) 10% noise level

Figure 6.15: Reconstructed parameters using inversion algorithm RNA-CKF and synthetic data, with 0%,5%,7%,10% white noise on the measurements and the regularization parameter $\alpha = 18$ and 5% noise on the initial state $\vec{x}_0$.

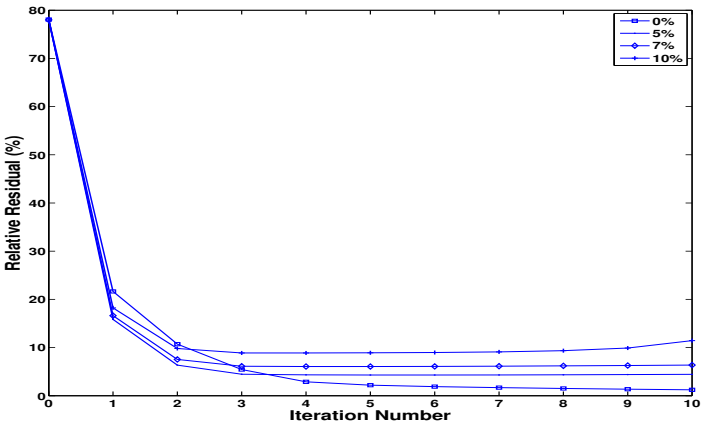

Figure 6.16: Convergence history for RNA-CKF with 5% noise on $\vec{x}_0$ and 0%,5%,7%,10% white noise on the measurements.

Chapter 7

Parameter Estimation Using Real Measurements: A Finger Tapping Experiment

In this chapter we use the RNA-CKF algorithm to estimate the parameters using the real fMRI measurements. Two sets of experiments were performed. The first set of experiments were performed with no noise on the initial state, however in the seconds set of experiments we assume 5% noise on the initial state $\vec{x}_0$. We performed all the experiments with the raw real data with 25 data points and the enriched data with 720 data points.

7.1 Description of the Data

One male subject was imaged while performing a finger tapping tasks. The study was approved by the Institutional Review Board (IRB) at Nationwide Childrens Hospital, Columbus, OH.

Scanning Sequences: fMRI was performed with a 3.0T GE Medical Systems Signal Excite and the BOLD sensitive T2* weighted echo-planar (EPI) sequence [43] using an 8 channel array head RF coil. Scanning protocol included a screening brain MR scan, including sagittal T1- weighted and axial T2- weighted scans, to exclude any anatomic brain abnormality. The task was performed with the following parameters: TE = 35 ms; TR = 3 s; flip angle = 90° single shot; full k-space, 128x128 acquisition matrix with a field of view (FOV) = 25.6 cm, generating an in-plane resolution of 2 mm2 and slice thickness of 8 mm with a max total of 20 axial slices. A total of 120 volumes (time points) were acquired.

Stimulation Protocol: The subject was instructed to begin and stop finger tapping every 30 seconds. Head motion was restricted by firm cushions packed around the head and by use of a head strap. The protocol followed a standard block design. The *On-Off* cycle was repeated six times for each scanning plane.

Data Processing: fMRI data preprocessing was carried out using FEAT (FMRI Expert Analysis Tool) Version 5.98, part of FSL (fMRIBs Software Library, `www.fmrib.ox.ac.uk/fsl`). Motion correction using MCFLIRT [27], mean-based intensity normalization of all volumes by the same factor, and temporal high-pass filtering (using 60 secs) was then performed on the data as well as spatial smoothing of 5 mm (Gaussian) were applied as pre-statistics processing. The time series for each voxel was then extracted for further analysis.

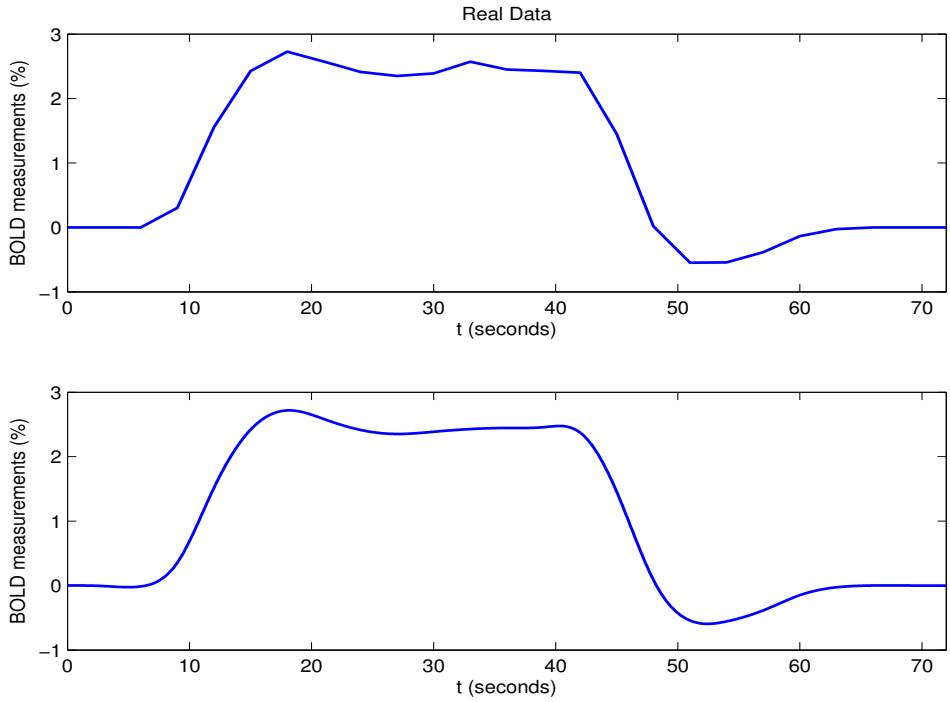

Figure 7.1: Real BOLD signal with 25 data points (top). Real BOLD signal with 720 data points (bottom).

The final measurements are over 72 seconds, with 25 data points that is every 3 seconds one measurement has been taken. Then by using interpolation (interp function in MATLAB) number of measurements have been increased to 720 points that is one measurement every 0.1 seconds. Figure 7.1 shows the two profiles.

7.2 Numerical Results

We applied the proposed inversion algorithm RNA-CKF to both sets of real measurements. We started by taking the same blind initial guess for $\vec{\theta}_0$ from the synthetic data experiment. We have used the regularization parameter $\alpha = 15$ for the first set of data and $\alpha = 500$ for the second set with 720 data points both obtained through the trial and error procedure. Figure 7.5 shows the reconstruction for the BOLD signal and the parameters.

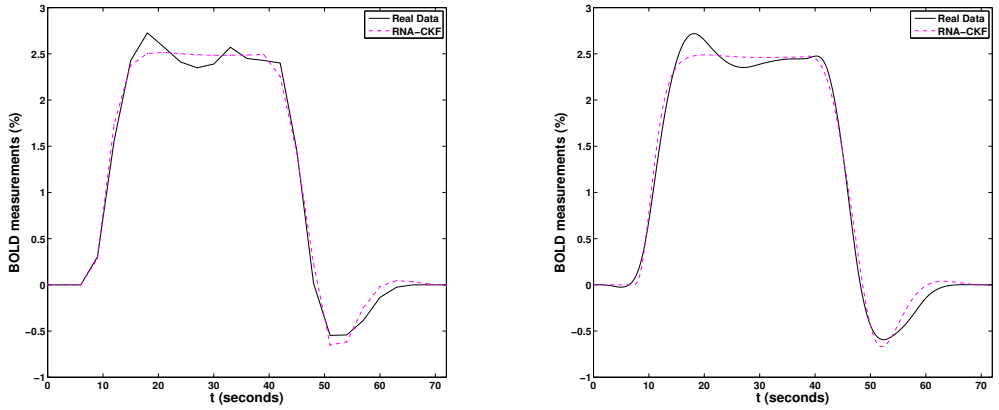

Figure 7.2: Reconstructed BOLD signal using inversion algorithm RNA-CKF and real measurements with 25 data points using regularization parameter $\alpha = 15$ (left). Reconstructed BOLD signal using inversion algorithm RNA-CKF and real measurements with 720 data points with $\alpha = 500$ (right).

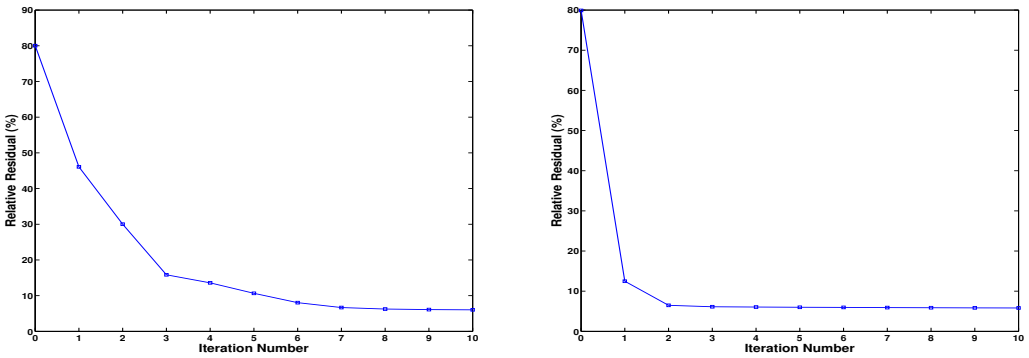

Figure 7.3: Convergence history for real data with 25 data points using regularization parameter $\alpha = 15$ (left). Convergence history for real data with 720 data points using regularization parameter $\alpha = 500$ (right).

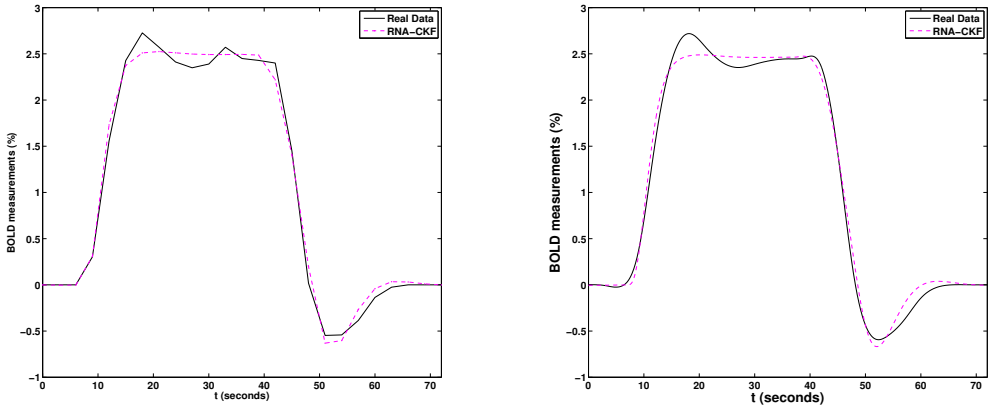

Figure 7.4: Reconstructed BOLD signal using inversion algorithm RNA-CKF and real measurements with 25 data points using regularization parameter $\alpha = 15$ (left). Reconstructed BOLD signal using inversion algorithm RNA-CKF and real measurements with 720 data points with $\alpha = 500$ (right).

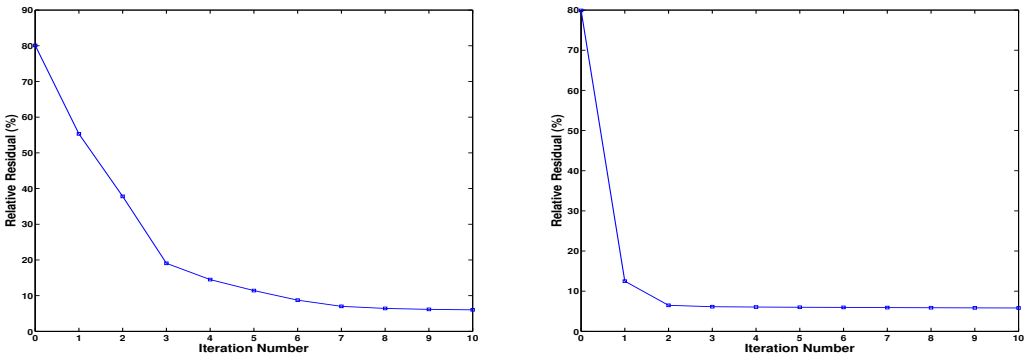

Figure 7.5: Convergence history for real data with 25 data points using regularization parameter $\alpha = 15$ (left). Convergence history for real data with 720 data points using regularization parameter $\alpha = 500$ (right), with 5% noise on the initial state $\vec{x}_0$.

Chapter 8

Conclusion

We have investigated mathematically and numerically the problem of estimating the biophysiological parameters of the Balloon model from the BOLD signal measurements. Solving this inverse problem appears to be a prerequisite step for understanding as well as monitoring brain responses to exogenous stimulus during brain activation.

From a mathematical point of view, we have performed a sensitivity analysis of the brain responses to the biophysiological parameters of the brain model. In particular, we have established a uniqueness result that can be viewed as an important step toward establishing the uniqueness of the solution of the considered inverse problem.

From a numerical point of view, we have designed an efficient solution methodology to estimate the biophysiological parameters in order to fit the dynamical system output (the BOLD signal). The main features of this technique are: (a) The regularized Newton algorithm that addresses the nonlinearity and restores the stability of the problem, and (b) The Cubature Kalman Filtering procedure for treating the noise on the measurements. Unlike existing methods, our proposed algorithm performs well even in the absence of a priori knowledge on the initial value of the parameters, as well as in the presence of noise on the initial state. We have obtained very promising results which demonstrate the robustness and the efficiency of the proposed inverse solver. Additionally, we have successfully applied our algorithm to calibrate the Balloon model from some measured BOLD signal extracted from fMRI images corresponding to a finger tapping experiment.

It is worthwhile to observe that the proposed method is conceptually easy to understand and is fairly straightforward to implement. The algorithm, coded in C, can run on a personal desktop or a laptop.

As stated in the introduction section, the goal of our research effort is to contribute to the understanding of brain activity and to provide the required tools to diagnose physical and psychological diseases at early stages. Our obtained results represent an interesting progress toward achieving this goal. Nevertheless, there are still many questions that remain without answers. Examples of such issues that need to be addressed in the short term run:

- The uniqueness of the solution of the considered inverse problem which will give

confidence for accurately targeting the parameters during the calibration process, especially when the data are contaminated with noise.

- A priori error estimates on the dependence of the state variables with respect to the parameters. These estimates will help better understand and quantify the sensitivity of the responses to the changes in the biophysiological parameters.
- Convergence results that are important for making the designed algorithm to be used in an automatic way. This kind of user friendly software will be then accessible to physicians and practitioners.

References

[1] Ienkaran Arasaratnam and Simon Haykin. Cubature kalman filters. *Automatic Control, IEEE Transactions on*, 54(6):1254–1269, 2009.

[2] Kwong KK Baker JR Davis TL Rosen BR Weisskoff RM. Boxerman JL, Bandettini PA. The intravascular contribution to fmri signal change: Monte carlo modeling and diffusion-weighted studies in vivo. *Magn Reson Med.*, 34(1):4–10, Jul 1995.

[3] R. B. Buxton and L. R. Frank. A model for the coupling between cerebral blood flow and oxygen metabolism during neural stimulation. *Journal of Cerebral Blood Flow and Metabolism*, 17:64–72, 1997.

[4] Richard B. Buxton, Kmil Uludaü, David J. Dubowitz, and Thomas T. Liu. Modeling the hemodynamic response to brain activation. *NeuroImage*, 23, Supplement 1(0):S220 – S233, 2004. ¡ce:title¿Mathematics in Brain Imaging¡/ce:title¿.

[5] Wong E. C. Buxton R. B. and Frank L. R. Dynamics of blood flow and oxygenation changes during brain activation: The balloon model. *Magn Reson Med*, 39:855–864, 1998.

[6] Mackey S. Chapin H, Bagarinao E. Real-time fmri applied to pain management. *Neurosci Lett.*, 520(2):174–81, Jun 2012.

[7] P. Ciuciu, J.-B. Poline, G. Marrelec, J. Idier, C. Pallier, and H. Bendali. Unsupervised robust nonparametric estimation of the hemodynamic response function for any fMRI experiment. *IEEE Transactions on Medical Imaging*, 22:1235–1251, 2003.

[8] Rebecca A. Clay. Functional magnetic resonance imaging: A new research tool. American Psychological Association, 750 First Street NE, Washington, DC 20002-4242, March 2007.

[9] Kress R. Colton D. *Inverse problems for partial differential equations*. Springer Verlag, 1992.

[10] T. Deneux and O. Faugeras. Using nonlinear models in fMRI data analysis: model selection and activation detection. *NeuroImage*, 32:1669 – 1689, 2006.

[11] De Freitas N. Gordon N. Doucet, A. *Sequential Monte Carlo methods in practice*. Springer Verlag, 2001.

[12] P. T. Fox and M. E. Raichle. Focal physiological uncoupling of cerebral blood flow and oxidative metabolism during somatosensory stimulation in human subjects. *National academy of science–proceeding*, 83:1140–1144, 1986.

[13] K J Friston. Bayesian estimation of dynamical systems: an application to fMRI. *NeuroImage*, 16(2):513–30, June 2002.

[14] K J Friston. Variational filtering. *NeuroImage*, 41(3):747–66, July 2008.

[15] K. J. Friston, P. Fletcher, O. Josephs, A. P. Holmes, M. D. Rugg, and R. Turner. Event-related fMRI: characterizing different responses. *NeuroImage*, 7:30–40, 1998.

[16] K. J. Friston, P. Jezzard, and R. Turner. Analysis of functional MRI time-series. *Human Brain Mapping*, 1:153–171, 1994.

[17] K. J. Friston, O. Josephs, G. Rees, and R. Turner. Nonlinear event-related responses in fMRI. *Mag.Reso. Med.*, 39:41–52, 1998.

[18] K J Friston, N Trujillo-Barreto, and J Daunizeau. DEM: a variational treatment of dynamic systems. *NeuroImage*, 41(3):849–85, July 2008.

[19] K. J. Friston, E. Zarahn, O. Josephs, R. Henson, and A. Dale. Stochastic design in event-related fMRI. *NeuroImage*, 10:607–619, 1999.

[20] K.J. Friston, A. Mechelli, R. Turner, and C.J. Price. Nonlinear responses in fmri: The balloon model, volterra kernels, and other hemodynamics. *NeuroImage*, 12(4):466 – 477, 2000.

[21] Rachael M. E. Euchring J. O. Grubb, R. L. and M. M. Ter-Pogossian. The effects of changes in pco2 on cerebral blood volume, blood flow and vascular mean transit time. *Stroke*, 5:630 – 639, 1974.

[22] J. Hadamard. *Lectures on Cauchy's problem in linear partial differential equations*. New Haven, Yale University Press, 1923.

[23] M. Havlicek, K. J. Friston, J. Jan, M. Brazdil, and V.D. Calhoun. Dynamic modeling of neural responses in fMRI using cubature kalman filtering. *Neuroimage*, 56:2109–2128, 2011.

[24] Martin Havlicek, Karl J. Friston, Jiri Jan, Milan Brazdil, and Vince D. Calhoun. Dynamic modeling of neuronal responses in fmri using cubature kalman filtering. *Neuroimage.*, 56(4):2109–28, Jun 2011.

[25] Z. Hu, X. Zhao, H. Liu, and P. Shi. Nonlinear analysis of the BOLD signal. *EURASIP journal on Advances in Signal Processing*, 2009, 2009.

[26] Scott Huettel. *Functional magnetic resonance imaging*. Sinauer Associates, Sunderland, Mass, 2008.

[27] Mark Jenkinson, Peter Bannister, Michael Brady, and Stephen Smith. Improved optimization for the robust and accurate linear registration and motion correction of brain images. *Neuroimage*, 17(2):825–841, Oct 2002.

[28] Eung Je Woo Jin Keun Seo. *Nonlinear Inverse Problems in Imaging*. Wiley, December 2012.

[29] Leigh a Johnston, Eugene Duff, Iven Mareels, and Gary F Egan. Nonlinear estimation of the BOLD signal. *NeuroImage*, 40(2):504–14, April 2008.

[30] Sergey Kabanikhin. *Inverse and Ill-posed Problems. Theory and Applications*. De Gruyter, 2011.

[31] Jane Campbell Langleben, Daniel D.; Moriarty. Using brain imaging for lie detection: Where science, law, and policy collide. *Psychology, Public Policy, and Law*, 19(2):222–234, May 2013.

[32] Khammash M Lillacci G. Parameter estimation and model selection in computational biology. *PLoS Comput Biol*, 6(3):e1000696, 2010.

[33] M Lindquist and T. Wager. Modeling the hemodynamic response function using inverse logit functions. In *Proceedings of Human Brain Mapping Annual Meeting*, 2005.

[34] Joe Malkevitch. Mathematics and the brain. *AMS*, 2013.

[35] J. B. Mandeville, J. J. A. Marota, C. Ayata, G. Zaharchuk, M. A. Moskowitz, B. R. Rosen, and R. M. Weisskoff. Evidence of a cerebrovascular postarteriole windkessel with delayed compliance. *Journal of Cerebral Blood Flow and Metabolism*, 9:679–689, 1999.

[36] Paul M. Matthews, Garry D. Honey, and Edward T. Bullmore. Applications of fmri in translational medicine and clinical practice. *Nat Rev Neurosci*, 7(9):732–744, 09 2006.

[37] Lawrence Murray and Amos Storkey. Continuous Time Particle Filtering for fMRI. *Advances in Neural Information Processing Systems*, 20:1–8, 2007.

[38] President Obama. Brain initiative. 2013.

[39] S. Ogawa, T. M. Lee, A. S. Nayak, and P. Glynn. Oxygenation-sensitive contrast in magnetic resonance image of rodent brain at high magnetic fields. *Magnetic Resonance in Medicine*, 14(1):68–78, April 1990.

[40] S Ogawa, R S Menon, D W Tank, S G Kim, H Merkle, J M Ellermann, and K Ugurbil. Functional brain mapping by blood oxygenation level-dependent contrast magnetic resonance imaging. A comparison of signal characteristics with a biophysical model. *Biophysical journal*, 64(3):803–12, March 1993.

[41] J. L. Boxermao B. R. Rosen R. M. Weisskoff, C. S. Zuo. Microscopic susceptibility variation and transverse relaxation: theory and exper- iment. *Magn. Reson. Med.*, 31:601–610, 1994.

[42] J. C. Rajapakse, E. Kruggel, J. M. Maisog, and D. Y. von Cramon. Modeling hemodynamic response for analysis of functional MRI time-series. *Human Brain Mapping*, 6:283–300, 1998.

[43] Ziad S Saad Rasmus M. Birn and Peter A Bandettini. Spatial heterogeneity of the nonlinear dynamics in the fmri bold response. *NeuroImage*, 826:817–826, 2001.

[44] J. J. Riera, J. Watanabe, I. Kazuki, M. Naoki, E. Aubert, T. Ozaki, and R. Kawashima. A state-space model of the hemodynamic approach: nonlinear filtering of bold signals. *NeuroImage*, 21:547–567, 2004.

[45] Suresh B. Srinivasamurthy. Methods of solving ill-posed problems. 2012.

[46] Albert Tarantola. *Inverse Problem Theory and Methods for Model Parameter Estimation*. Society for Industrial and Applied Mathematics, 2005.

[47] V. Y. Tikhonov, A. N.; Arsenin. *Solutions of Ill-Posed Problems*. Winston, New York, 1977.

[48] Curtis R. Vogel. *Computational Methods for Inverse Problems*. Society for Industrial and Applied Mathematics, Philadelphia, PA, USA, 2002.

[49] Haacke E. M. Yablonsky D. A. Theory of nmr signal behavior in magnetically inhomcigflnous tissues: the static dephasing regime. *Magn. Reson. Med.*, 32:749–763, 1994.

[50] Petrov Yuri P. and Valery S. Sizikov. *Well-posed, Ill-posed, and Intermediate Problems with Applications*. De Gruyter, Berlin, Boston, 2005.

Chapter 9

Appendix: Brain Imaging with fMRI

Functional magnetic resonance imaging or functional MRI (fMRI) is an MRI procedure that measures brain activity by detecting associated changes in blood flow. This technique relies on the fact that cerebral blood flow and neuronal activation are coupled. When an area of the brain is in use, blood flow to that region also increases. The primary form of fMRI uses the Blood Oxygen Level Dependent (BOLD) signal discovered by Seiji Ogawa [1]. This is a type of specialized brain and body scan used to map neural activity in the brain or spinal cord of humans or other animals by imaging the change in blood flow (hemodynamic response) related to energy use by brain cells. Since the early 1990s, fMRI has come to dominate brain mapping research because it does not require people to undergo shots, surgery, or to ingest substances, or be exposed to radiation [26].

The procedure is similar to MRI but uses the change in magnetization between oxygen-rich and oxygen-poor blood as its basic measure. This measure is frequently corrupted by noise from various sources and hence statistical procedures are used to extract the underlying signal. The resulting brain activation can be presented graphically by color-coding the strength of activation across the brain or the specific region studied. The technique can localize activity to within millimeters but, using standard techniques, no better than within a window of a few seconds. fMRI is used both in the research world, and to a lesser extent, in the clinical world. It can also be combined and complemented with other measures of brain physiology such as EEG[2] and NIRS[3]. Some companies have developed commercial products such as lie detectors based on fMRI techniques, but the research is not believed to be ripe enough for widespread commercialization [31].

The process starts with a stimulus which causes the neural activation. Following increased neural activity in the brain, the local cerebral blood flow (CBF) increases much more than the cerebral metabolic rate of oxygen ($CMRO_2$), and as a result local oxygen extraction fraction (E) decreases with activation [12]. Because the local blood is more oxygenated, there is less deoxyhemoglobin present, the magnetic field distortions are reduced, and the local MR signal increases slightly. This small blood oxygenation level dependent (BOLD) signal change is the mapping signal used in most functional magnetic resonance

[1] Seiji Ogawa (January 19, 1934) is a Japanese researcher known for discovering the technique that underlies Functional Magnetic Resonance Imaging (fMRI)

[2] EEG: Electroencephalography

[3] NIRS: Near-infrared spectroscopy

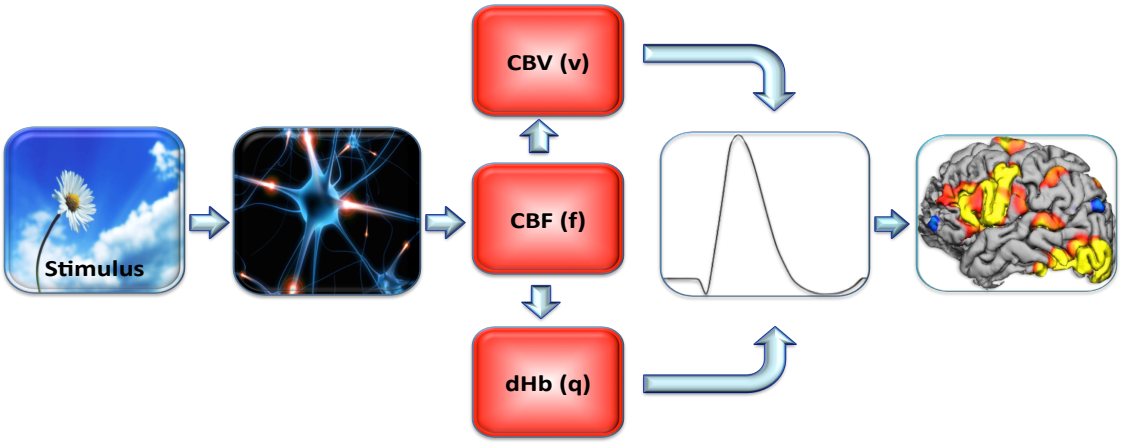

Figure 1: From stimulus to BOLD signal and fMRI image[4].

imaging (fMRI) applications [4].

fMRI vs. MRI

If you are having your brain scanned with MRI, you lie on a table with your head inside a giant magnet. Protons inside the atoms in your brain align themselves with the magnetic field, only to be whacked temporarily out of alignment by a pulse of radio wave aimed at your head. As protons relax back into alignment again, they themselves send out radio waves that a computer uses to create a brain snapshot.

Whereas with fMRI, researchers rely on two more facts about the body: the fact that blood contains iron (and we know that the main function of iron is to carry oxygen in the body) the second fact is that blood rushes to a specific part of the brain that is activate. As freshly oxygenated blood zooms into a region, the iron that carries the oxygen distorts the magnetic field enough for the scanner to pick up the signal [8]. Therefore in fMRI, patients don't need to be exposed to radiation or ingesting substances. Overall, fMRI has many advantages

	MRI	fMRI
Structural Images	✓	✓
Functional Images	✗	✓
3D Images	✗	✓
Radiation-free	✗	✓
Shot-free	✗	✓
No Substances Ingested	✗	✓

Table 1: fMRI vs. MRI

[4]Brain image courtesy of Dr. Ned T. Sahin, Multi-Modal Imaging Lab, UCSD.

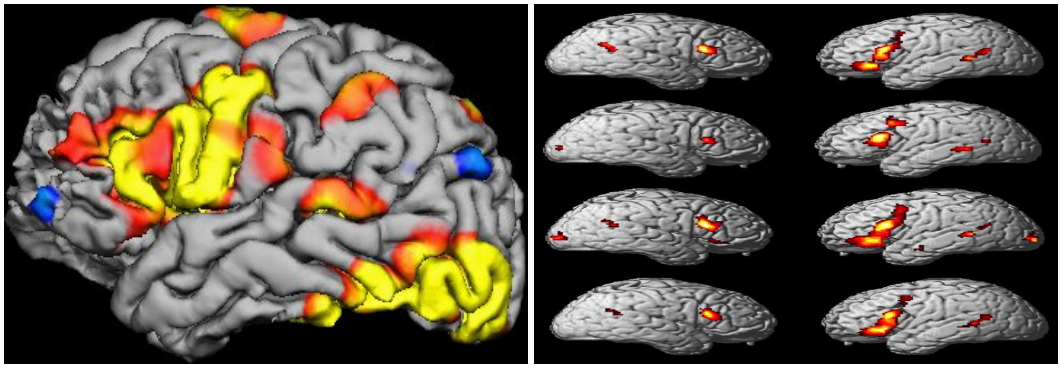

Figure 2: fMRI is used to locate activated area in the brain.

over MRI, Table 1 summarizes these properties.

Applications

fMRI has had a major impact in cognitive neuroscience. fMRI now has a small but growing role in clinical neuroimaging, with initial applications to neurosurgical planning. Current clinical research has emphasized novel concepts for clinicians, such as the role of plasticity in recovery and the maintenance of brain functions in a broad range of diseases. There is a wider potential for clinical fMRI in applications ranging from pre-symptomatic diagnosis, through drug development and individualization of therapies, to understanding functional brain disorders. Realization of this potential will require changes in the way clinical neuroimaging services are planned and delivered [36].

fMRI is being used in areas including but not limited to:

1. Tracking visually guided response

   Using fMRI images, scientist can study visually guided responses and detect the area of the brain related to the visual responses (see Figure 3), so these important tissues can be avoided during brain surgeries.

2. Pain management studies

   Current views recognize the brain as playing a pivotal role in the arising and maintenance of pain experience. Real-time fMRI (rtfMRI) feedback is a potential tool for pain modulation that directly targets the brain with the goal of restoring regulatory function. Though still relatively new, rtfMRI is a rapidly developing technology that

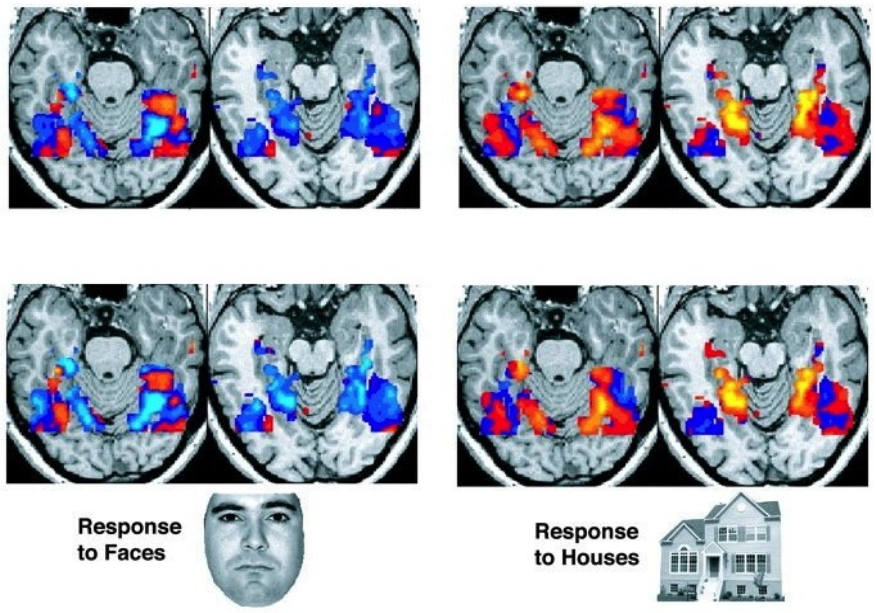

Figure 3: fMRI images show different brain response to different images[5].

has evolved in the last 15 years from simple proof of concept experiments to demonstrations of learned control of single and multiple brain areas [6]. Figure 4 illustrates the reduced paint related brain activity by using virtual reality during treatments of burn patients.

3. Risk assessment: Potential role of fMRI is in directing decisions about surgical and diagnostic procedure.

4. Language generation studies: fMRI was also used to identify candidate language processing areas in the intact human brain.

5. Complex problem solving.

6. Comprehension of sequential information.

7. fMRI is also used to detect the effect of:

   (a) detect the effect of tumors, strokes and brain diseases and how the brain recovers after stroke.

[5]Source:`http://en.wikipedia.org/wiki/Functional\_magnetic\_resonance\_imaging`, accessed January 30, 2013.

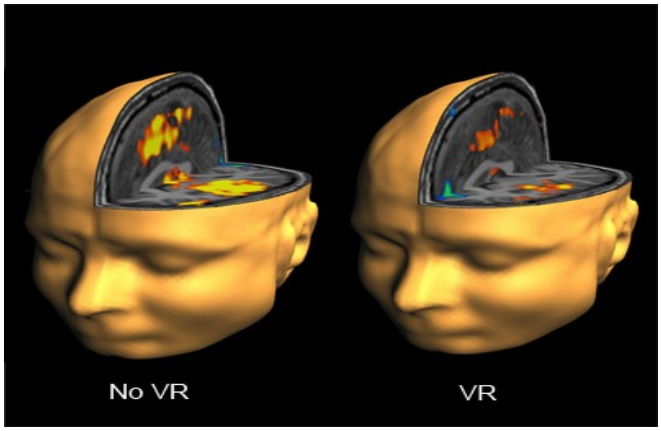

Figure 4: Reduced pain related brain activity[6].

(b) head injuries.

(c) psychological disorders such as Alzheimer's and depression.

(d) drugs and behavioral therapy.

[6]Image courtesy of Dr. Hunter Hoffman, Human Interface Technology Laboratory, University of Washington